

Molecular Beam Epitaxy Growth and Properties of Fe_3GeTe_2 Thin Films

by

Ryan Lee Roemer

B.Sc., The University of California, Santa Cruz, 2017

A THESIS SUBMITTED IN PARTIAL FULFILLMENT OF
THE REQUIREMENTS FOR THE DEGREE OF

MASTER OF SCIENCE

in

The Faculty of Graduate and Postdoctoral Studies

(Physics)

THE UNIVERSITY OF BRITISH COLUMBIA

(Vancouver)

April 2021

© Ryan Lee Roemer 2020

The following individuals certify that they have read, and recommend to the Faculty of Graduate and Postdoctoral Studies for acceptance, the thesis entitled:

Molecular Beam Epitaxy Growth and Properties of Fe_3GeTe_2 Thin Films

submitted by **Ryan Lee Roemer** in partial fulfillment of the requirements for the degree of **Master of Science in Physics**.

Examining Committee:

supervisor name

Ke Zou, University of British Columbia (Physics and Astronomy)

additional examiner name

Alannah Hallas, University of British Columbia (Physics and Astronomy)

Abstract

Monolayer iron germanium telluride Fe_3GeTe_2 , one of the typical two-dimensional ferromagnetic materials, hitherto, has only been studied by exfoliated micron-sized samples. We achieve high-quality wafer-scale growth of thin Fe_3GeTe_2 films by molecular beam epitaxy, greatly expanding the types of characterization tools employable and providing the possibility for its integration in devices like consumer electronics. Thickness-dependent transport measurements are used to characterize and probe for magnetic order. Ferromagnetic states exist in 1–10 layer thick Fe_3GeTe_2 , with Curie temperatures ranging from 75 K in one layer samples to above 175 K in ten layer samples. A single ferromagnetic phase with significant magnetic anisotropy is revealed for all layer numbers. We present the capability of synthesizing, wafer-scale Fe_3GeTe_2 as an essential step towards its fulfillment in any applications involving magnetism, such as spintronics.

Lay Summary

When layers of Fe_3GeTe_2 are grown in impurity free environments we are able to study the underlying physics of such a system free of the physics associated with defects. When these crystals are grown with precision it is possible to control the number of layers size and shape leading to natural integration into devices. However, the growth of such crystals is no easy task. In this thesis we discuss the trials, failures and successes of the first growth of ultra-thin films of Fe_3GeTe_2 revealing the intrinsic nature of the phase transition from the ferromagnetic to paramagnetic states.

Preface

The work presented in this thesis was conducted during my tenure as a masters student researcher at the University of British Columbia under the supervision of professor Ke Zou. It has involved collaboration with many members of this group. I specify this involvement, as well as other collaborations and resulting publications which are detailed in this thesis. Much of Ch. 1 and 4 is work conducted in UBC's Thin Film Laboratory by myself, Dr. C. Liu, and Professor Ke Zou. published as R.L. Roemer, C. Liu, K. Zou. Robust ferromagnetism in wafer-scale monolayer and multilayer Fe_3GeTe_2 , npj 2D Materials and Applications volume 4, 53 (2020). It details the growth and characterization of Fe_3GeTe_2 thin films grown by molecular beam epitaxy.

As the lead researcher on this project, I designed the project, grew the films, carried out measurements, and wrote the manuscript. Chong Liu provided theoretical as well as experimental guidance and Ke Zou oversaw and suggested the project. The two collaborators provided valuable feedback during the writing of the manuscript.

Table of Contents

Abstract	iii
Preface	v
Table of Contents	vi
List of Tables	viii
List of Figures	ix
Acknowledgements	xiii
Dedication	xiv
1 Theoretical background of few quintuple layer Fe_3GeTe_2	1
2 Experimental Techniques & Design	5
2.1 Molecular Beam Epitaxy Technology	5
2.2 Transport Measurements	9
2.3 Atomic Force Microscopy	14
2.4 Diffraction	15
3 Growth Process; Exploring the Parameter Space	21
3.1 Sapphire FGT growth	26
3.2 Ge FGT growth	33
3.3 Capping Decapping	42
4 Experimental results	48
4.1 Structural Characterization of Pristine FGT Samples by Co- Deposition	48
4.2 Transport results showing the conductivity and ferromag- netism in Fe_3GeTe_2 films	52
4.3 Temperature dependence of the anomalous Hall behavior	54

Table of Contents

5 Discussion & Conclusion	60
Bibliography	62

List of Tables

- 2.1 Table of effusion Cells in both growth chambers in Zou's Lab. Those above the double horizontal line live in Growth Module 1 (GM1) those below are placed in Growth Module 2 (GM2). 7

List of Figures

2.1	Examples of common shapes and sizes of MBE crucibles. All crucibles included above are made of pyrolytic boron nitride.	8
2.2	A non-exhaustive categorization of the conductive states yielded by transport data	10
2.3	A cartoon schematic of indium cold welded pad geometry placed on the sample surface.	11
2.4	Post antisymmetrization the hysteresis loop shows signs of the normal Hall effect as indicated by the linear part of the loop at high magnetic field values.	13
2.5	A typical hysteresis resulting from a transverse resistance measurement.	14
2.6	An example of the experimental setup of an 2θ - ω scan.	16
2.7	Bragg scattering off a plane of atoms in a crystal.	17
2.8	Common surface defects and their corresponding RHEED diffraction pattern signatures.	20
3.1	Lattice structure of Fe ₃ GeTe ₂	22
3.2	The crystal structure of sapphire (Al ₂ O ₃)	23
3.3	AFM scan of the sapphire surface exemplifying islands left on the substrate surface.	24
3.4	Sapphire cleaned with methanol only.	24
3.5	AMF height profile of the sapphire (0001) surface.	25
3.6	AFM scan of sapphire cleaned with acetone, isopropyl alcohol, and methanol.	26
3.7	RHEED images of the sapphire surface along the two crystallographic directions where a) and c) belong to the [10 $\bar{1}$ 0] direction and b), d) belong to the [11 $\bar{2}$ 0] direction. Top sub-figures are pre-annealed substrates and the bottom sub-figures are post-annealed RHEED images. Note: the RHEED intensity dramatically increases after annealing at high temperature.	27
3.8	RHEED image of the first attempt at FGT growth.	29

List of Figures

3.9	Line profiles of sapphire substrates and possible films.	30
3.10	RHEED images of a polycrystalline film grown on the sapphire (0001) surface.	31
3.11	RHEED image of polycrystalline sample with 3D character.	32
3.12	Examples of RHEED images with varying amounts of Te flux in codeposition growth.	33
3.13	The first truly 2 dimensional RHEED images obtained during shutter growth on sapphire.	34
3.14	RHEED images of Ge samples in the two unique crystallographic directions.	36
3.15	2θ - ω scan from 0-100 deg. of the Ge(111) surface.	37
3.16	RHEED images of FGT shutter method of 10 UC of FGT and other phases.	37
3.17	XRD 2θ - ω scan from 0-90 degrees of shutter growth method of a 10 UC film on Ge (111).	38
3.18	$2 \times 2 \mu\text{m}$ AFM image of a 10 UC FGT surface grown on Ge(111).	39
3.19	Transport data of FGT shutter method of 10 UC of FGT and other phases.	40
3.20	RHEED images of FGT co-deposition method of 2 UC of FGT and other phases.	40
3.21	2θ - ω scan of a 10 UC co-deposited FGT film on Ge(111).	41
3.22	$2 \times 2 \mu\text{m}$ AFM image of the FGT surface grown on Ge(111).	42
3.23	Transport data of 10 UC FGT grown via codeposition with other phases.	43
3.24	RHEED images of FGT film and Te cap.	44
3.25	RHEED image of film post Te decapping experiments.	45
3.26	RHEED images of a) 2 UC FGT sample and b) amorphous Se cap.	45
3.27	RHEED image of a 2×1 reconstructed film surface during the Se decapping procedure.	46
3.28	RHEED images of the Se decapped FGT films.	46
4.1	In-situ RHEED images of a 2×2 reconstructed Ge (111) substrates and FGT films	49
4.2	RHEED intensity oscillations during the growth of Fe_3GeTe_2	50
4.3	Ex-situ XRD of the out-of-plane lattice structure of FGT films.	51
4.4	Diffuse scattering FGT sample after exposure to ambient conditions for only a few minutes.	52
4.5	A photo of an FGT sample measuring the longitudinal resistance with van der Pauw geometry in a PPMS	53

List of Figures

4.6	Longitudinal resistivity R_{xx} vs. temperature T taken of various QL numbers.	54
4.7	Fit of the R_{xx} with the Mott variable range hopping model, indicating the existence of localized states below 125 K. . . .	55
4.8	R_{AH} vs. applied field of select QL numbers at 5 K showing the hysteresis loops belonging to the AH measurement.	55
4.9	Anomalous Hall resistance of a single-QL, b 2-QL, c 5-QL, and d 10-QL FGT films.	56
4.10	Transverse resistance measurement analysis.	58

List of Acronyms

- 2D - 2-Dimensional
- 3D - 3-Dimensional
- AH - Anomalous Hall
- AFM - Antiferromagnetic
- AHE - Anomalous Hall Effect
- ARPES - Angle-Resolved Photoemission Spectroscopy
- DI - Deionized Water
- FM - Ferromagnetic
- FGT - Fe_3GeTe_2
- GM1 - Growth Module 1
- GM2 - Growth Module 2
- HF - Hydrofluoric Acid
- IPA - Isopropyl Alcohol
- MAE - Magnetocrystalline Anisotropy Energy
- MBE - Molecular Beam Epitaxy
- MRAM - Magnetic Random Access Memory
- NC - Non-Capped
- PB - Parallel Beam
- PBN - Pyrolytic Boron Nitride
- PG - Pyrolytic Graphite
- PMA - Perpendicular Magnetic Anisotropy
- PPMS - Physical Properties Measurement System
- QL - Quintuple Layer
- RAH - Anomalous Hall Resistance
- RHEED - Reflection High Energy Electron Diffraction
- RMS - Root Mean Square
- RR - Reminent Resistance
- RS - Saturation Resistance
- SC - Sticking Coefficient
- STM - Scanning Tunneling Microscopy
- UC - Unit Cell
- UHV - Ultra High Vacuum
- VdW - Van der Waals
- XRD - x-Ray Diffraction

Acknowledgements

I would like to thank Dr. Chong Liu for his outstanding dedication to my scientific growth, Bruce Davidson, Fengmiao Li, Ted Shin and Simon Godin for their thoughtful discussions and scientific insight. Finally I would like to thank Professor Ke Zou for giving me a place to grow both literally and figuratively.

Dedication

I dedicate this work to my mother, Melissa Robin Roemer, whose love and care I will remember and carry through my life. Besos y abrazos.

Chapter 1

Theoretical background of few quintuple layer Fe_3GeTe_2

It is possible that the future of information storage and spintronics lies within 2-dimensional (2D) magnetic materials [1]. Spin transfer torques can change the magnetization direction to control these systems. The ability to control magnetic states electronically via spin transfer torques originates at the interface. 2D materials pose potential for the increased density of interfaces, as the surface-to-volume ratio becomes larger in reduced dimensions, making them desirable in applications. The ability to tune 2D materials to display desired characteristics is also much greater. For example, strains can be tuned in 2D, where 3-dimensional (3D) materials are of fixed bond lengths. This is important when constructing heterostructures where strains can be used to increase interface compatibility. Another beneficial property of 2D materials is their stability in monolayer forms. The interlayer bonding is Van der Waals, thus the surfaces are free of dangling bonds. The same cannot be said of 3D materials where cleaving the largely ionic bonding between layers often leaves the surface covered in dangling bonds. The ability to tune magnetic order is also much greater in 2D materials as the magnetic order is more robust in 3D materials, making manipulation of such orders much more difficult. Magnetic metals, semiconductors and insulators all have prospects in applications. In magnetic insulators, long spin wave propagation lengths are desired as well as the reduction in ohmic losses. 2D materials also show strong proximity effects when coupled with 2D semiconductors yielding a way to control an extra degree of freedom: valley polarization [2]. This degree of freedom has yet to be thoroughly explored outside of a few materials.

In the transition metal trihalides, particularly the Cr trihalides, all bulk samples, exhibit ferromagnetic order within layers with out-of-plane easy-axis directions for CrI_3 and CrBr_3 and in-plane for CrCl_3 [3–5]. CrCl_3 also exhibits antiferromagnetic interlayer magnetic order. The weak antiferromagnetic coupling between the layers gives rise to extremely large tunnel magnetoresistance [6].

In 3D, the integration of magnetic materials into electronic and photonic devices has been taking place for decades [7–9]. One well-known example is the discovery of giant magnetoresistance and its applications [10]. Much research has focused on engineering new magnetic structures, especially in two-dimensions (2D). Prospects of which are plentiful in device application, not only in replacing magnets in current applications, but also in new structures, such as in magnetic tunnel junctions and magnetic random access memories (MRAM) [11, 12].

The discovery of graphene [13] inspired a new generation of materials known as Van der Waals (VdW) materials with intrinsic 2D nature [14]. Samples were often accessible by exfoliating bulk crystals. After being processed as a device, the electronic properties of these 2D materials could be controlled via strain, doping, gating, as well as “stacking” [15], to reveal exotic states leading to an era of “VdW materials by design” [16]. Fundamental physical properties have been realized that were proposed long-ago [17, 18], in 2D VdW materials, including the 2D superconductivity found in thin films of NbSe₂ [19], FeSe [20], WTe₂ [21], and Bi₂Sr₂CaCu₂O₈ [22]. New opportunities in applications and a new generation of devices have become available due to the properties found in reduced dimensions.

Exfoliated 2D flakes of CrI₃ [23], Fe₃GeTe₂ [24], Cr₂Ge₂Te₆ [25], and others [26] have shown clear long-range magnetic order that are promising for applications involving properties such as above-room-temperature Curie temperature (T_c) and antiferromagnetic interlayer exchange.

The library of such materials has recently grown drastically, and can be classified as belonging to one of two categories; the transition metal halides and the transition metal chalcogenides. For example, the transition metal dihalides MX₂ and transition metal trihalides MX₃ have become extremely popular as they have been shown to display a large range of magnetic behaviours.

Ferromagnetic (FM) order has been observed in both localized and itinerant materials where all examples have out-of-plane magnetization. Examples of which include the transition metal halides and chalcogenides [1]. The kinds of Antiferromagnetic (AFM) order in 2D has become quite extensive. AFM zigzag, stripe, A-type and Neel AFM has been observed in various stoichiometries of transition metal halides and tertiary chalcogenides [1] In these materials, the transition metal (usually belonging to the 3D row) are arranged in a triangular lattice and bonded to nonmagnetic anions in the halide column, namely iodine, chlorine and bromine. In these compounds, the halide atoms are stacked adjacent between layers in multiple configurations. The magnetic moments originating from the transition metal ion’s

spin and orbital angular momentum, interact via superexchange where the first, second and third nearest neighbor superexchange interactions have been shown to be important in determining the kinds of magnetic order [27]. The superexchange is also quite sensitive to the cation anion bond angle and length.

2D intrinsic magnetic order in a topological insulator has been observed in Manganese bismuth telluride ($MnBi_2Te_4$) [28]. The crystal structure is composed of a setuple layer structure which demonstrates in-plane A type AFM order below 25 K [28] and FM order in-plane which undergo a spin-flop transition to a canted out-of-plane antiferromagnetic state.

Yet, scalability and poor stability continue to hinder the progression toward the realization of the industrial-scale production of such devices [26]. To date, the synthesis of many 2D magnetic materials still is all limited to micron-sized flakes [29], eliminating any production scale applications. Here we focus on the wafer-scale synthesis of the VdW layered FM material Fe_3GeTe_2 (FGT), which has a T_c above room temperature [24] and is one of the few 2D magnetic materials that shows evidence of topological states [30, 31].

Single-crystal FGT was synthesized in 2006 [32], revealing a relatively high T_c of $\sim 220K$ in bulk, in comparison to the absence of magnetism in the isostructural Ni_3GeTe_2 . This material has an out-of-plane magnetization vector with respect to the VdW planes in the ordered state [33], showing a large anisotropy defined as the energy dependence on the magnetization vector direction. Calculations indicate its easy-axis is stabilized by a large magnetocrystalline anisotropy caused by spin-orbit coupling [34]. Angle-resolved photoemission spectroscopy (ARPES) measurements imply the FGT bulk belongs to a class of topological nodal line semimetals [35]. Another ARPES experiment suggests the FM state is accompanied by a heavy-fermion state, which has only been seen in 4 f and beyond electron systems [36].

Exfoliated FGT monolayers and multilayers [24, 37] preserve the characteristic FM order of bulk. T_c reaches 310K upon ionic liquid gating in trilayer samples [24], one of the highest FM transitions recorded among known 2D materials. Unlike CrI_3 , no interlayer exchange coupling has been observed in FGT films. It has been shown that FGT hosts a large Berry curvature, which is responsible for the anomalous Hall effect (AHE) [35]. Thin-film measurements substantiate claims of topological properties in the observation of Néel-type skyrmions in FGT/ WTe_2 heterostructures and large anomalous Nernst effect [31, 38].

Until recently, FGT films remained the only metallic, rare-earth free, and

layered FM with out-of-plane magnetization in 2D. Because of the metallic characteristics, its fundamental magnetic properties can be studied via transport measurements, together with optical measurements such as the magneto-optic Kerr effect. Metallicity also enables easy control of charge as well as spin degrees of freedom by electrical currents, useful in device applications. For example, FGT films have been made into ultrathin devices, realizing current control of the perpendicular magnetization via spin-orbit torque, with efficiencies comparable to that of 3D FM heterostructures—the current leader of the field [39]. This makes FGT all the more desirable for magnetic random access memory (MRAM) [40]. Closely related application prospects are found in magnetic tunnel junction heterostructures of FGT/graphite/FGT, which display promising characteristics of 160% tunneling magnetoresistance at low temperature [41].

We employ the molecular beam epitaxial technique to synthesize atomically smooth and single crystalline FGT films, with thickness ranging from one quintuple layer (a single QL, also the smallest substructure of FGT, ~ 0.8 nm) to ten QLs on 5×5 mm substrates. Among reported monolayer samples, ours display the highest T_c probed by AH measurements, together with an order of magnitude larger coercivity [24, 42]. Large switching ratios have been found in all samples at low temperatures as well as significant magnetocrystalline anisotropy. Our wafer-scale samples yield the opportunity for measurements and applications, which can be extremely difficult on the micron-sized flakes yielded by exfoliation techniques, such as ARPES and x-ray spectroscopies. One can begin integrating FGT films into commercial devices following the established techniques of silicon.

Chapter 2

Experimental Techniques & Design

2.1 Molecular Beam Epitaxy Technology

Ultra High Vacuum

In this work, we focus on the growth of 2D materials using state-of-the-art technology known as, molecular beam epitaxy (MBE). MBE takes place in stainless steel chambers which are kept in high or ultra high vacuum (UHV) environments which we define as pressures ranging from 10^{-3} to 10^{-8} torr, and less than 10^{-8} respectively. These pressures result in gas densities of the order 10^{13} and 10^7 mol/cm³ respectively. To contrast this point the density of molecules in ambient conditions is roughly 2×10^{21} mol/cm³. In UHV few species of atoms remain, the majority of which are CO, N₂ and H₂. At pressures so low the mean free path of atoms and molecules, which survive in the chamber, approaches the tens of miles. These densities allow for growth of the most pristine, impurity-free films accessible to date which are required not only to study and disentangle fundamental physics from that of disorder and impurities, but are also necessary for the semiconducting industry today.

To achieve such low pressures, specialized vacuum pumps are required. To approach UHV, it is common to use a roughing and turbo pump in sequence and often others such as cryopumps and ionpumps are necessary. Even then, specialized pumps may be required to further vacate the chamber.

Sources, Source Materials and Evaporation Techniques

In MBE, pure source materials are epitaxially transported to the sample surface in the gaseous state. The technique used to sublimate the sources varies, and depends on parameters such as the vapor pressure of an element in the liquid and solid state. Some elements require sub-zero temperatures

2.1. Molecular Beam Epitaxy Technology

to maintain the solid state, while others are required to be heated past 1000 °C before the vapor pressure yields a measurable atomic flux. In general, elements with d and f shell valence states have higher melting points where s and p shell elements tend to have lower melting points (with the exception of some mono- and divalent p series elements). Fortunately, a variety of techniques have been developed to satisfy such requirements. For the majority of elements, a crucible is sufficient in holding the source materials. In Zou's lab, three volumes of crucible are used, 5 cc, 10 cc and 30 cc. A common but non-exhaustive list of such materials which crucibles are made include alumina, graphite, pyrolytic boron (PBN), pyrolytic graphite (PG), tantalum, titanium, and tungsten based on the material placed inside. For our purposes, we use conical crucibles with exceptions for Se. These crucibles are wrapped with resistive heaters and monitored by thermocouples to achieve atomic sublimation and maintain consistent flux. The combination of heaters crucibles and thermocouples are often referred to as "cells".

Cells are further characterized by the number of filaments and types of elemental metals used in their construction. High temperature-low vapor pressures source materials require refractive metals to operate and are referred to as high temperature cells. Single filament cells or low temperature cells operate between 100°C and 750°C and have a small thermal mass to ensure stability. This is particularly important when dealing with high vapor pressure materials because slight variations in thermal energy can result in relatively large changes in atomic flux.

Dual filament cells allow one to regulate different zones of the crucible. For example, during the growth of aluminum containing compounds, the lip of the crucible is kept cooler than the base. This ensures the source materials remain inside the crucible and refrain from wetting any other MBE components. In Zou's lab we strictly use single filament cells.

Single filament high temperature cells operate up to 2000°C while ensuring constant temperature stability. This is enabled by high purity tungsten and tantalum hot zone at the base of the crucible.

For specialty elements such as chalcogenides, a cracker is used. Currently a 500 cc valved cracker is used in the Zou lab for Se in the growth of Se containing films. Selenium will vaporize as Se₂ similar to O₂, as they both have the same valence state. Thus, after the initial sublimation from bulk Se to diatomic Se, the atomic flux is carried through a region where the walls may be maintained at a higher temperature relative to the bulk state, such that when diatomic selenium undergoes a collision with the walls, it "cracks" in two and becomes atomic selenium, which is then epitaxially delivered to the sample surface. The cracker also is equipped with a needle valve such

2.1. Molecular Beam Epitaxy Technology

Material	Cell Type	Crucible
Sr	30cc Low Temp	PBN
Bi	30 cc Standard	PBN
Nd	10cc High Temp	W
La	10 cc High Temp	W
Ni	10 CC High Temp	W + BeO
Eu	30 cc Standard	PBN
Ti	10 cc High Temp	W
Te	30cc Low Temp	PBN
Ge	30cc Standard	PBN
Fe	10 cc High Temp	W + Al ₂ O ₃

Table 2.1: Table of effusion Cells in both growth chambers in Zou’s Lab. Those above the double horizontal line live in Growth Module 1 (GM1) those below are placed in Growth Module 2 (GM2).

that the high vapor pressure material may be completely isolated from the growth chamber and an atomic flux can be more easily regulated.

For convenient reference the table 2.1 reports the current state of the sources and crucibles in our dual GENxplor system.

Veeco manufactures other crucible types but for our purposes these options suffice. These crucibles are further customizable in the material as to adhere to each materials specific needs. Elements with high melting points such as tungsten W ($\sim 3000^{\circ}\text{C}$) require special procedures to sublimate the material like an electron beam evaporator.

Substrates

In the MBE chamber, materials are deposited onto another crystal known as the substrate. This crystal, as discussed below, is a key choice in the growth process. Most importantly, it provides a template to grow. We can break the substrate and film relationship into two categories: epitaxial and non-epitaxial growth. Non-epitaxial growth is a growth where the film and substrate have little to no coherence. In epitaxial growth the substrate is chosen such that the film grows in the orientation of the substrate. This is done by choosing a substrate with similar in-plane lattice constants. The film then adheres to the substrate such that each unit cell falls onto some integer multiple of the unit cells of the substrate. In this work many substrates are



Figure 2.1: Examples of common shapes and sizes of MBE crucibles. All crucibles included above are made of pyrolytic boron nitride. Figure adopted from [43]

used.

Strain & Interface Engineering

This template can be chosen such that the film and substrate have similar lattice constants which we then expect the film to grow epitaxially on the surface. Although the film growth may be epitaxial, minute differences in lattice constants will lead to in-plane strain on the film.

In this case, substrates not only provide a template to grow the target material, but can often lead to new physics due to a variety of reasons. The substrate can be chosen to either stretch or compress the film. This allows one to explore physics that may be emergent given a proper strain. Oftentimes this leads to interesting phenomena in otherwise banal system. These strains are broken into two categories: compressive and tensile strain. Compressive strain indicates the films in-plane lattice constants are slightly smaller than those of the chosen substrate. Tensile strain implies the opposite. The induced strain can often lead to new behaviors or changes in physical properties of the film. As the film becomes thicker and more unit cells are deposited, the strain begins to relax through a variety of mechanisms, eventually relaxing to its bulk values.

Preparation to Ensure Atomically Clean Surfaces

Oftentimes substrates arrive from distributors with dirty surfaces. Dirty here meaning atomically rough or littered with contaminants such as organics on the surface. To rid the surfaces of such contaminants various etching procedures are used. These procedures often require the use of extremely acidic solutions like HCl or H₂SO₄, but many contaminants can be removed with volatile chemicals such as acetone and ethanol.

To make the substrates atomically smooth high temperature annealing processes may be required either in UHV or with flows of ultra-pure gasses such as O₂ or HAr.

2.2 Transport Measurements

All transport measurements were carried out in a Quantum Design physical properties measurement system (PPMS), where Van der Pauw geometry was used to measure longitudinal (R_{xx}) and transverse (R_{xy}) resistances. Contacts were made via indium cold pressing and attached via a gold wire.

Van der Pauw

The Van der Pauw geometry is a common technique to probe the resistance of approximately 2D samples. In this limit, the technique allows one to probe samples of arbitrary shape granted the film is continuous with a negligible amount of holes. In this design, four contacts are placed on the perimeter of the film. Although this approach does not measure resistivity of a specified area, it yields a resistance averaged over the entirety of the film. This may be a problem for anisotropic materials, but in MBE atomic, uniformity is assumed over the entire growth area. The four contact placement allows for multiple types of measurements from which properties may be extracted. Such properties and the techniques to extract them are detailed below.

Longitudinal Geometry

Resistances may be measured in a number of different geometries and each geometry probes for a unique property. Longitudinal resistance quantifies the insulating, conducting or semiconducting properties of a material. The measurement is often performed as a function of temperature where a continuous current is supplied between two contacts, while the remaining pair of contacts measures the potential difference on the same surface as shown

2.2. Transport Measurements

by Figure 2.3 a). This allows one to decouple the contact resistance from the intrinsic resistance of the sample. As the current is passed through the sample, voltage is read at each temperature to determine the resistive behavior of the sample. The resistance of a sample may be used to categorize it in term of its resistivity as shown in Figure 2.2

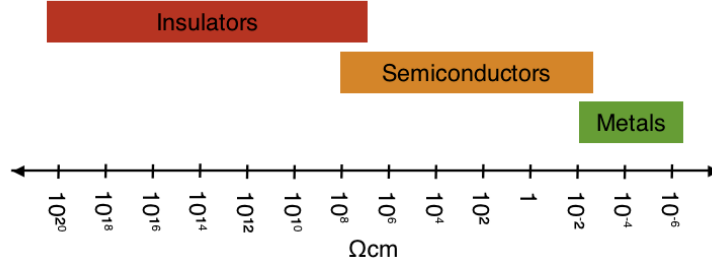


Figure 2.2: A non-exhaustive categorization of the conductive states yielded by transport data adopted from [44].

Sheet resistance

Many thin films, especially Van der Waal's materials, show conductivity within sheets. One helpful way to analyze materials is by the resistance we expect to be in a 2D planes. For example, in a 2D electron gas, it is not obvious what the thickness of the conducting plane is, thus we analyze the resistance in terms of sheet resistance. The units of such are ohms. Many VdW materials are quasi 2D electron gasses. Thus sheet resistance can be helpful in extracting properties such as carrier density and mobility.

$$R = \frac{\rho}{t} \frac{L}{W} = R_S \frac{L}{W} : R_S = \frac{\rho}{t} \quad (2.1)$$

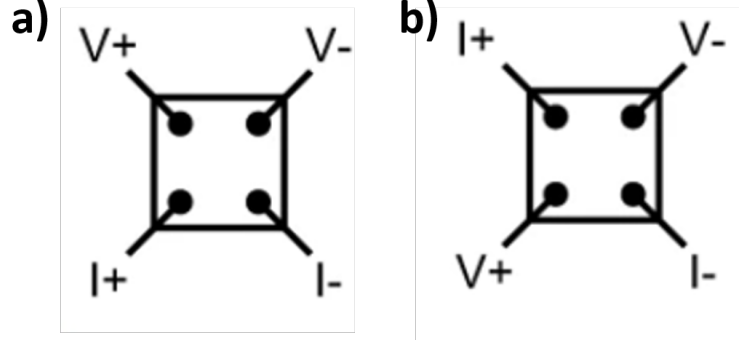


Figure 2.3: a) A cartoon schematic of indium cold welded pad geometry placed on the sample surface. Note the V+, V- and I+, I- groups lie in parallel, indicating a longitudinal geometry. V and I stand for current and voltage respectively. b) A cartoon schematic of transverse pad geometry placed on the sample surface. Note the V+, V- and I+, I- groups are orthogonal indicating a transverse geometry. V and I stand for current and voltage respectively.

Here R is the measured resistance, ρ is the resistivity, L , and W are the length and width of the sample respectively and R_S is the sheet resistance.

Transverse geometry

Hall Resistance

Another useful quantity that is commonly extracted from transport measurements in the Van der Pauw geometry is the Hall resistance. The Hall resistance yields valuable information such as the type of carrier (i.e. electrons or holes) as well as the concentrations of such carriers. The Hall resistance is a result of the Hall effect, in which a current subject to an applied magnetic field leads to the eventual buildup of carriers on one side of the sample due to the Lorentz force detailed in Figure 2.2

$$\mathbf{F} = q(\mathbf{E} + \mathbf{v} \times \mathbf{B}) \quad (2.2)$$

The direction of the resulting voltage is determined by the carriers in the sample. By fitting the linear portion of the transverse resistance in the anomalous Hall measurement detailed below, it is possible to extract the Hall coefficient. It is possible to describe the Hall resistance in terms of the

current density and in turn the carrier density of single carrier materials as follows. Let us define a sample subject to out-of-plane magnetic B field in the positive z direction, while current I is carried in the positive x direction.

$$R_H = \frac{E_y}{j_x B} = \frac{1}{ne}$$

(2.3)

Anomalous Hall Measurements

Thin films can be notoriously difficult to measure using standard magnetometry, this is due to the relatively small number of magnetic atoms relative to bulk.

In metallic materials, such as Fe_3GeTe_2 , this challenge can be circumvented with transport measurements. To do this, one places contacts in the transverse Van der Pauw geometry, identical to a Hall measurement as shown in Figure 2.3 b). Samples are then cooled and may experience a structural magnetic or electronic phase transition. Once a desired temperature is reached, the samples are then isothermally exposed to a magnetic field while current is ran through the sample. The applied field is swept through a desired cycle (usually a few T). In an intrinsic ferromagnet this measurement theoretically results in a transverse resistance signal,

$$R_{xy} = R_N(H) + R_{AH}(M) \quad (2.4)$$

where R_{xy} is the measured signal from the PPMS (H) is the applied field R_N is the normal Hall resistance(H) is the applied field. Magnetization is then related to the second term where R_{AH} is the AH coefficient and (M) is the magnetic signal from the sample

The AHE occurs in solids where spin-orbit coupling exists, which breaks the time-reversal symmetry. Multiple mechanisms are theorized to play a role, including Berry-phase related physics and disorder related phenomena. Berry phase AHE are said to dominate in metallic ferromagnets with low conductivity which is the case for Fe_3GeTe_2 .

Raw data yielded by experiment are usually not antisymmetric as one would expect from a non-interacting magnetic hysteresis. These shapes are due to imprecise pad geometry, in other words, a typical R_{xy} measurement contains R_{xx} components. Thus raw data were first antisymmetrized to remove the R_{xx} component, according to

2.2. Transport Measurements

$$R_{H\uparrow}(B) = [R_{xy\uparrow}(+B) - R_{xy\downarrow}(-B)]/2 \quad (2.5)$$

and

$$R_{H\downarrow}(B) = [R_{xy\downarrow}(+B) - R_{xy\uparrow}(-B)]/2 \quad (2.6)$$

Here $R_{xy,\uparrow}$ and $R_{xy,\downarrow}$ are the values during the increasing and decreasing field sweep, respectively, and B is the applied magnetic field.

After such an antisymmetrization, the loops saturated resistances in the negative and positive field directions have equal magnitudes, as displayed in Figure 2.4. Here it is important to note the loops are centered about the origin, but there remains a linear portion with a non-zero slope where the loops have become saturated in the high field regions.

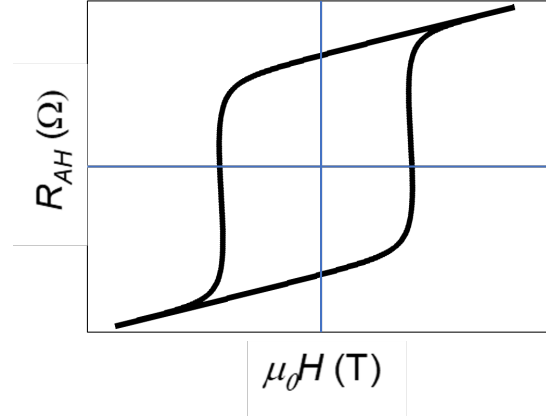


Figure 2.4: Post antisymmetrization the hysteresis loop shows signs of the normal Hall effect as indicated by the linear part of the loop at high magnetic field values.

This linear portion slope shown in Figure 2.4 is due to the normal Hall effect from which the Hall coefficient may be extracted to reveal the carrier type and concentration. In anomalous Hall experiments this contribution is removed. In this experiment the normal Hall coefficients were subtracted

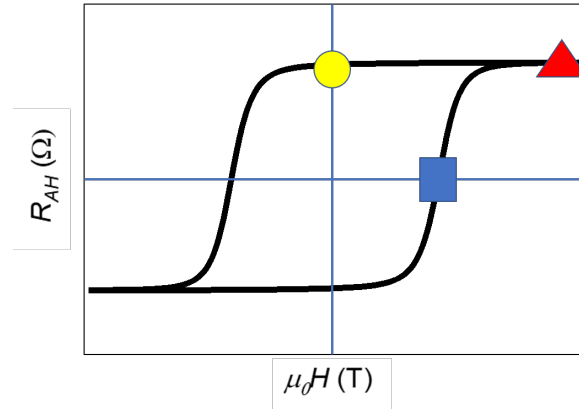


Figure 2.5: A typical hysteresis resulting from a transverse resistance measurement. Note: the non-zero slope of the saturated linear portion of the hysteresis and the non-symmetric position of the loop due to the R_{xx} contribution and non-exact pad placement. The yellow circle indicates the value of the remanant resistance, the red triangle indicates the value of saturation resistance and the blue square is the coercive field

by fitting the magnetically saturated portion of the data with a term proportional to the applied field. What remains is an anomalous resistance, which is directly related to the intrinsic magnetization, an example of which is plotted in Figure 2.5. Here is an example of a magnetic hysteresis loop obtained from anomalous Hall measurements on a film in the FM state after symmetrization and decoupling tricks have been performed. Labeled in the figure are a few quantities that may be noted. The yellow circle represents the remanent resistance, the red triangle marks the saturation resistance and the blue square is the coercive field value.

2.3 Atomic Force Microscopy

Atomic force microscopy (AFM) is a kind of scanning probe microscopy capable of imaging sample surfaces at the nanometer scale. In our experiments, we used a tapping-mode technique to avoid contamination and destruction of the sample surface. The apparatus operates using a silicon tip usually micrometers in diameter, placed at the end of a cantilever, which then oscillates vertically (z direction). The oscillations of the cantilever reflect a laser to a detector as the tip scans in the x - y plane. Deflections from these oscil-

lations due to electrostatic forces between the tip and sample are recorded and used to map the sample surface via an image by assembling lines of horizontal scans.

In our experiment, AFM was helpful to investigate the surface topography of substrates to ensure atomic smoothness in hopes of obtaining atomically flat films of such substrates. It was also beneficial in determining the effects of pre-growth etching and annealing procedures.

2.4 Diffraction

In the Zou lab, samples are probed with x-ray diffraction (XRD) ex-situ. From X-ray diffraction, one is capable of determining the film thickness, crystal structure and in the case of heterostructure growth, the superlattice period. In this experiment, high energy photons are emitted from a Cu anode. The Cu anode is the target of the electrons which knock out core electrons. Outer electrons drop down to fill the empty orbital and emit x-rays. The photons emitted are not monochromatic. In our case, both α_1 and α_2 emission channels are used, with wavelengths of 1.5406\AA and 1.544425\AA respectively. According to our diffraction conditions these two wavelengths result in a superposition of two diffraction peaks. In theory, this results in a tightly spaced double peak. In practice, these peaks are extremely difficult to resolve at low angles, thus the average wavelength of the two peaks is used to determine lattice constants. Some diffractometers are equipped with a monochromator which suppresses the α_2 emission channel. The trade off here being the total intensity is diminished, but the probing wavelength is exact, allowing for a more precise determination of the lattice parameters. This minute difference in lattice parameters can be problematic as some imprecision caused by the mixed wavelengths can be of similar order of magnitude as the question at hand in cases such as determining relaxations, and differences in bulk and thin film structures.

Once emitted from the anode, the photon is diffracted by the sample. The incident beam penetrates a few microns due to the energy of the photons. This is why substrates often generate the largest peak intensities (many orders of magnitude larger than the film). The majority of the diffracted beam penetrates a few microns below the surface, a great deal deeper than the usual thicknesses of films. To further highlight this point, signals from the metal sample holder can also be observed. This is why samples are placed on an anti-reflective Ge(111) zero-diffraction disk which prevents secondary diffraction processes. Once diffracted, the photons travel

to a detector.

For the purposes of this thesis 2θ - ω scans were performed. In this technique, both the detector and source are coupled and move symmetrically throughout the scan as displayed in Figure 2.6. Note: ω is not necessarily equal to $\frac{1}{2} * 2\theta$ because there is an intrinsic offset of the sample. This offset originates from the substrate having its diffraction vector (marked S in Figure 2.6) offset with respect to the normal of the sample holder. This could be due to miscuts of the substrate or residual paste on the backside.

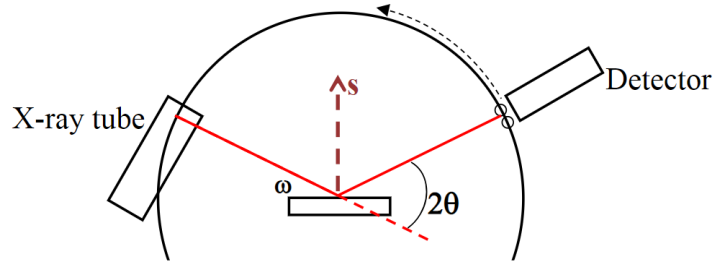


Figure 2.6: An example of the experimental setup of an 2θ - ω scan. Omega is defined as the angle of the beam with respect to the horizontal while 2θ is the angle of the incoming beam with respect to the detector. The diffraction vector marked S.

In 1913 Bragg & Bragg attributed the characteristic patterns of reflected X-rays to parallel planes of atoms, which composed the crystal. They hypothesized that such planes were equally spaced, and consequently, atoms reflecting x-rays would do so constructively and destructively based on the angle of incidence. For monochromatic light, constructive interference is only possible when an integral number of wavelengths fit in the extra distance a wave reflects off successive planes. This has become known as the Bragg condition, as shown in eq.2.7

$$n\lambda = 2d\sin\theta \quad (2.7)$$

Here n is an integer, λ is the wavelength of the incident photon, and θ is the angle of incidence measured from the lattice plane, as shown in Figure 2.7.

For the purposes of this thesis, XRD was used to determine out-of-plane lattice constants ex-situ.

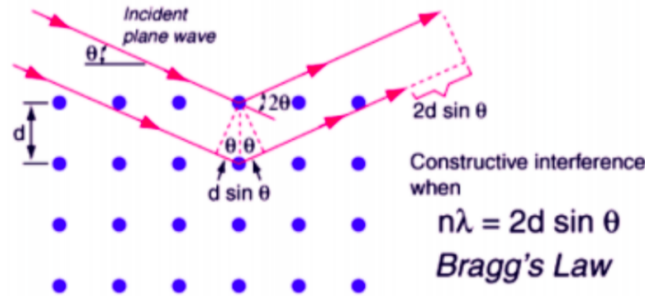


Figure 2.7: Bragg scattering off a plane of atoms in a crystal. Note: the extra distance traveled by the incident wave interacting with the lower plane is $2d\sin\theta$ figure adopted from [45].

RHEED

When growing materials with multiple elements, there may exist compounds with similar in-plane lattice constants and symmetries with different stoichiometries. Thus during growth, it is impossible to be determine what has been grown in-situ with 100% confidence. The uncertainty can be greatly diminished by measuring the in-plane lattice constants by diffraction.

During the growth process, a powerful tool to monitor the sample condition is reflection high energy electron diffraction (RHEED). It allows users to optimize stoichiometry as well as determine surface termination for layered materials. Contrary to XRD, this technique uses electrons emitted from an electron gun to diffract from the first few layers of a sample surface at grazing incidence (in some systems this process can be quite destructive). The diffracted electrons are then accelerated to a phosphorescent screen where a characteristic diffraction pattern is revealed. Thus the process is electron in, electron out. The diffraction patterns are a result of the wave-like nature of the electrons interacting with the periodic electric potential created by the array of atoms. To probe the crystal for its atomic structure the electrons wavelength must be comparable to that of the lattice spacing which is of the order of a few angstroms. The relationship between a particles momentum and wavelength is given by the de Broglie wavelength $\lambda = \frac{h}{mv}$ where h is the plank constant $h = 6.626 \text{ E } 34 \text{ m}^2\text{kg/s}$, m is the electron mass $9.109 \text{ E } 31 \text{ kg}$ which are both constants. Thus to control the de Broglie wavelength, the only free parameter we have to tune is the electron velocity, which is

2.4. Diffraction

controlled by the potential difference supplied by the RHEED apparatus. In our experiment, we use an energy of 15 KeV which results in an electron wavelength of 0.122 \AA . which is an order of magnitude less than most lattice spacing. With a sufficient potential difference supplied to accelerate electrons the next step is to generate enough electrons such that the patterns displayed on the phosphorescent screen is of adequate intensity. This is done via control of the emission current. In our experiment, we use an emission current of roughly $0.3 \mu\text{A}$, which is sufficient to characterize the diffraction pattern while avoiding the potential pixel burnout on our screen. In some samples containing highly volatile elements (those with high vapor pressure like Se) it is not uncommon to create vacancies in the material or completely destroy the lattice altogether. This must be kept in mind while adjusting the RHEED intensity and energy. Generating diffraction images without damaging samples has been eased by the data acquisition software in KSA 400 system. The program allows users to adjust the exposure time per frame as well as sum over multiple frames. The trade-off with this approach is, the growth process becomes less interactive because images are generated every few seconds rather than multiple images per second.

Often times the surface of a film will not resemble its bulk structure. Atoms on the surface will rearrange themselves to find a lower energy state which is commonly referred to as surface reconstruction. Fundamentally the rearrangement results from a discontinuity in the potential above the surface layer. Thus the anharmonic forces which determine the equilibrium positions move the atoms in either the lateral or vertical direction referred to as relaxation or reconstruction respectively. Relaxation among most metals brings the surface atoms closer to the existing crystal. In other words, the c lattice constant will slightly decrease for the surface layer. Intuitively this makes sense because the interlayer bonding below is not competing with a layer above. For a certain crystal structure there may be multiple reconstructions that emerge under various conditions (i.e. temperature). These reconstructions hint at long range order within the beam spot. The prototypical example of which is the 7×7 Si(111) reconstitution.

Because each crystal structure has a unique diffraction pattern, it is possible to extract various properties of the crystal under consideration. This is particularly important when growing crystals with MBE. For example, elements or compounds evaporated from crucibles may form multiple crystal structures when combined, sometimes with the same atomic flux. Luckily, RHEED is capable of distinguishing between phases with its multitude of tools. In many cases, the phases may be identified in-situ by their unique crystal structures and lattice parameters allowing for a more interactive

growth. Unfortunately, due to the grazing incidence, the c lattice parameter is inaccessible, yet in-plane lattice constants are accessible by analyzing the distances between diffraction spots. This approach is best done by comparing the known in-plane lattice constants of the bulk crystal substrate. In the KSA software there exists a pixel spacing tool in which users can place a line with variable width (to integrate and average) to quantitatively study the in-plane lattice spacing.

Upon growth of our 2D materials starting from a bulk substrate, it is possible to witness the diffraction pattern change in real time. This is because the underlying reciprocal space rods from the top layers reveal are replaced with those corresponding to the new material.

This situation presents the opportunity to analyze the as grown in-plane lattice constants. Because commercially available bulk substrates are usually of high quality, it is typical within the community to accept the well documented bulk lattice constants. This paired with a constant sample geometry allows one to trace the progression of lattice constants by simply noting the ratio of pixel spacing and known bulk constants. This provides an immediate check as to the in-plane constants.

Often times, coherently grown epitaxial films will naturally be strained due to lattice mismatch at the substrate/film interface. This strain will begin to relax after just a few layers and will eventually relax to its bulk lattice constants. This strain evolution can sometimes vary as much as 10% of the bulk lattice constants.

Surface defects can greatly influence the diffraction pattern. Qualitatively diffraction patterns may be characterized by the eye, as described in Figure 2.8 where common surface defects are listed with the corresponding changes to an otherwise ideal diffraction pattern in Figure 2.8.

The other important information such as the crystal symmetry can be found by RHEED. This is done by noting the number of unique diffraction patterns found after rotating the sample a complete revolution. Sample quality can often be inferred by the quality of the diffraction pattern. Streaky lines indicate 2D growth where point like diffraction spots indicate atomically smooth films.

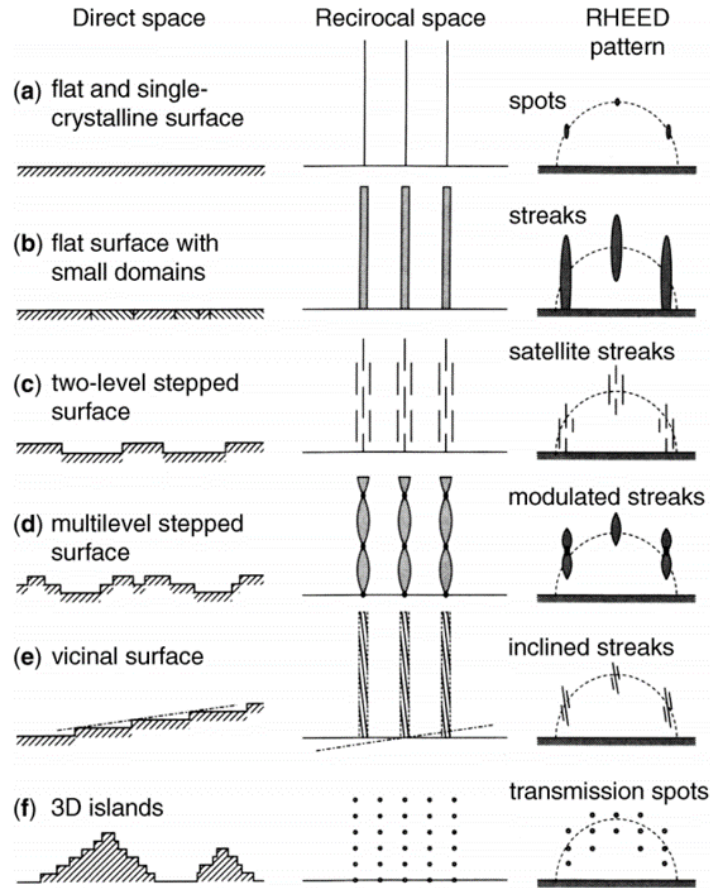


Figure 2.8: Common surface defects and their corresponding RHEED diffraction pattern signatures figure adopted from [46].

Chapter 3

Growth Process; Exploring the Parameter Space

In this chapter the unsuccessful growths of Fe_3GeTe_2 FGT will be discussed. Various parameters such as substrate temperature, atomic fluxes and growth periods will be explored. These trials provided valuable insight into the growth process and how to efficiently explore the parameter space. This chapter is provided for the reader such that future growths of similar compounds will be easier upon comparison to data presented. Conditions that ultimately led to the successful growth of FGT are discussed in chapter 4.

FGT films were synthesized using a Veeco GENxplor system. Standard effusion cells are mounted at the bottom of the chamber facing the same point at the center of the chamber where the substrate is facing downwards. Source materials of Fe (99.98%), Ge (99.999%), and Te (99.9999%) were evaporated from the effusion cells.

The FGT unit cell is described by a hexagonal symmetry (space group P63/mmc) composed by two weakly coupled quintuple layer (QL) substructures, with bulk lattice parameters $a = b = 3.99 \text{ \AA}$, and $c = 16.33 \text{ \AA}$, as shown in Figure 3.1. The middle three layers of each QL form a heterometallic slab of $\text{Fe}^{2+}\text{Ge}^{4-}$ surrounded by Fe^{3+} atoms. Encapsulating the slabs are tellurium layers. Theoretical calculations of monolayer magnetic moments yield Fe^{3+} and Fe^{2+} atoms contribute 1.723 and $1.005 \mu\text{B}$, respectively [34], where is the Bohr magneton. The structure is displayed in Figure 3.1

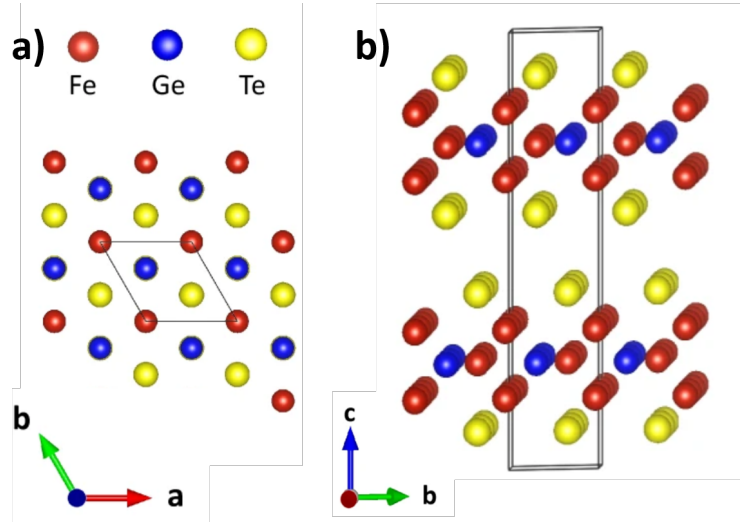


Figure 3.1: Lattice structure of Fe_3GeTe_2 (FGT), where a single unit cell (two quintuple layers (QL)) is outlined. a) top down view of the FGT unit cell and right: the lattice projected along the a axis. There exist two inequivalent Fe sites, Those closest to the tellurium layers have a 3+ oxidation state where those in the Ge layer have an oxidation state of 2+. The 3+ state are said to carry larger magnetic moment with respect to the 2+ state [34].

In early trials of the growth of FGT, Al_2O_3 (sapphire) was selected as the substrate of choice following suit of the only reports of MBE grown FGT as in reference [47]. Here the reader should note the alternating layer structure of sapphire and the inter layer distance of roughly 2 \AA . The commercially bought substrates were of (0001) termination. Yet, due to miscuts incurred during fabrication, the termination layer alternates between the A and B layers indicated in Figure 3.2. Although the in-plane symmetry of sapphire and FGT are both hexagonal, the in-plane lattice parameters of sapphire are $a=b=4.758 \text{ \AA}$ roughly 18% larger than that of FGT. From this large discrepancy it is safe to assume the film would not be coherently strained. Yet, sapphire is often a good substrate choice because it can be easily prepared to atomically smooth terraces and non-polar surface. Substrates were ordered from MTI Corp as well as Crystec. The differences between the two substrate supplied were mostly negligible, the only comment-able difference was the reported c axis parameter. From MTI the reported c lattice constant was

12.992 Å, while the Crystec c parameter was given to be 13.002Å. Fortunately this difference would not pose any problem. As both could eventually yield atomically flat surfaces. The original procedure used an initial wash

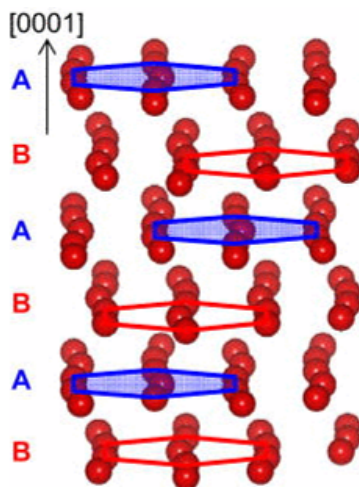


Figure 3.2: The crystal structure of sapphire (Al_2O_3) The unit cell is composed of 8 alternating A and B layers. The Lattice constants are $a=b=4.763$ Å, and $c=13.003$ Å. Figure adopted from [48]

in acetone followed by an isopropyl alcohol (IPA) wash in a sonicator for 3 minutes. The results left the surface rough as displayed in the AFM scan in displayed in Figure 3.3. A methanol wash was also performed and compared to the acetone and IPA. The results were slightly more desirable with less islands in a larger scan size as displayed in Figure 3.4. The resulting surfaces did not display atomic terraces conducive to growth.

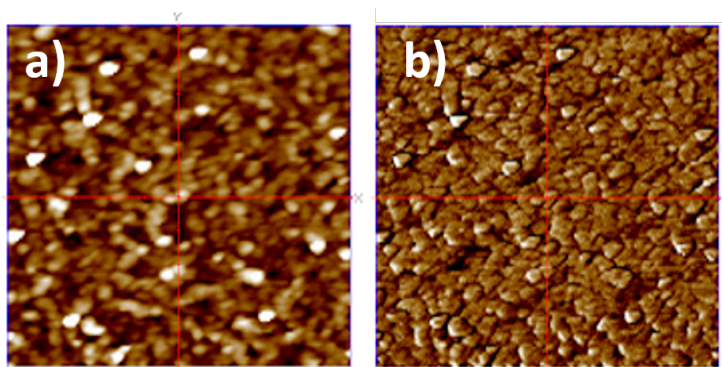


Figure 3.3: A $2 \times 2 \mu\text{m}$ AFM scan of the sapphire surface exemplifying islands left on the substrate surface. a) a forward height scan of the sapphire surface where islands are clearly visible as indicated by the round spots of brighter hue. b) the tapping phase in the forward direction which serves to highlight the non-uniformity of the surface.

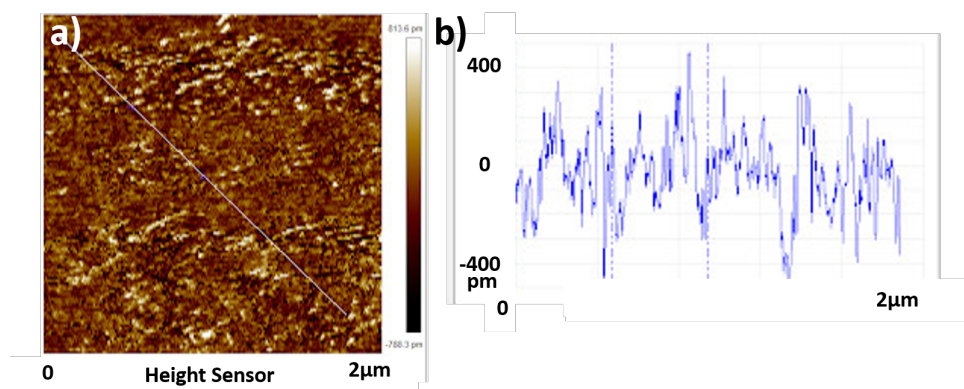


Figure 3.4: Sapphire cleaned with methanol only. a) A $2 \times 2 \mu\text{m}$ scan of the Sapphire surface. b) The height profile of the diagonal white line in a) the height profile ranges roughly 1000 pm over the entire scan. The RMS surface roughness is roughly 870 pm.

Because the surface did not display atomic terraces a high temperature annealing process was developed to reveal atomic terraces. Substrates were placed in a furnace with an oxygen flow at $1200 \text{ }^\circ\text{C}$ for 30 minutes. The

warm-up was linear at 6 °C/min and the cool-down was also linear at 4 °C/minute which resulted in nice atomic terraces, as displayed in Figure 3.5 in which the sapphire crystal demonstrates atomic terraces over the entirety of the scanned surface. The technique has further been developed using a methanol rise in the sonicator for 3 minutes repeated 3 times subsequently followed by the annealing procedures described above with corresponding scans displayed in Figure 3.6. The result was large atomically smooth terraces with no apparent surface decoration i.e. no islands. With the resulting substrates it was possible to begin the growth process.

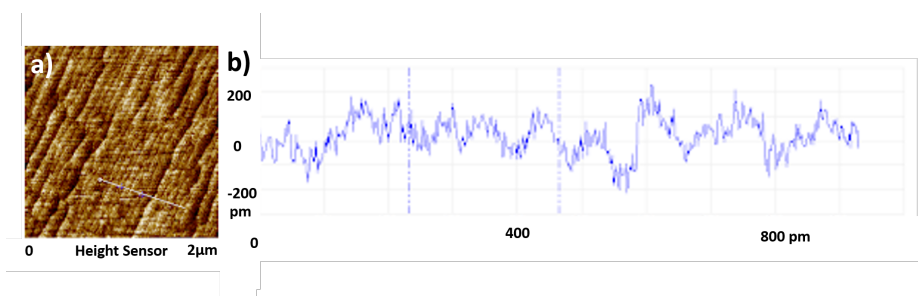


Figure 3.5: A $2 \times 2 \mu\text{m}$ AFM height profile of the sapphire (0001) surface. a) Clearly resolved atomic terraces. This sample was placed in the furnace at 1200C for 30 minutes. The heat-up and cool-down were over a 110 and 600 minute duration respectively. The image to the left is the height where darker represents low height and bright areas represent high portion. b) The height profile along the white line indicated in figure a) . The steps along the line correspond to a single atomic layer in the sapphire crystal along the c axis.

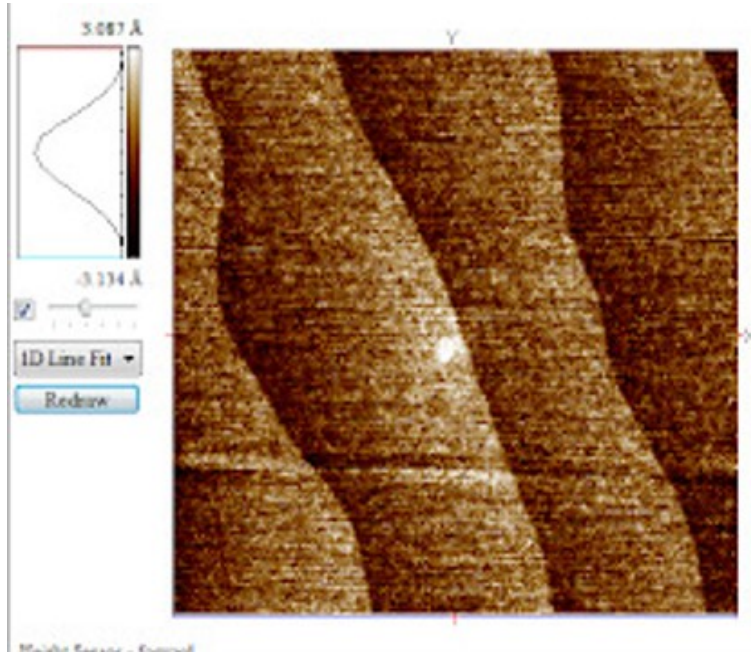


Figure 3.6: AFM scan of sapphire cleaned with acetone, isopropyl alcohol, and methanol followed by a high temperature annealing at $1120^{\text{circ}}\text{C}$ for 60 minutes. More specifically a 110 min heat-up, and 600 min cool-down. The height variation of the scan is roughly 6 Å.

3.1 Sapphire FGT growth

After the surfaces were cleaned, the substrates were ready to be degassed in UHV. Substrates were mounted on either tungsten or molybdenum circular sample holders with carbon paste that used water as a solvent and loaded into the loadlock chamber. In the loadlock chamber, substrates were heated by two argon gas filaments to 200°C for 2 hours. Prior to degassing, pressures were roughly 10^{-7} torr and after degassing would reach $\sim 10^{-9}$ torr. After the initial degassing procedure was completed, substrates were brought through the buffer chamber and into GM2, the chalcogenide growth chamber. In GM2, samples were further degassed at 600°C for 30 minutes. RHEED images were then taken of the two distinct crystallographic directions. The $[10\bar{1}0]$ direction as well as the $[11\bar{2}0]$ directions both pre-growth and post-growth as displayed in Figure 3.7. Here a) and b) correspond to

3.1. Sapphire FGT growth

pre-annealed substrates and c) and d) correspond to substrates annealed at 600°C for 30 minutes. a) and c) correspond to the $[10\bar{1}0]$ crystallographic directions, while b) and d) correspond to the $[11\bar{2}0]$ direction. All RHEED images were taken with a 0.3 A emission current.

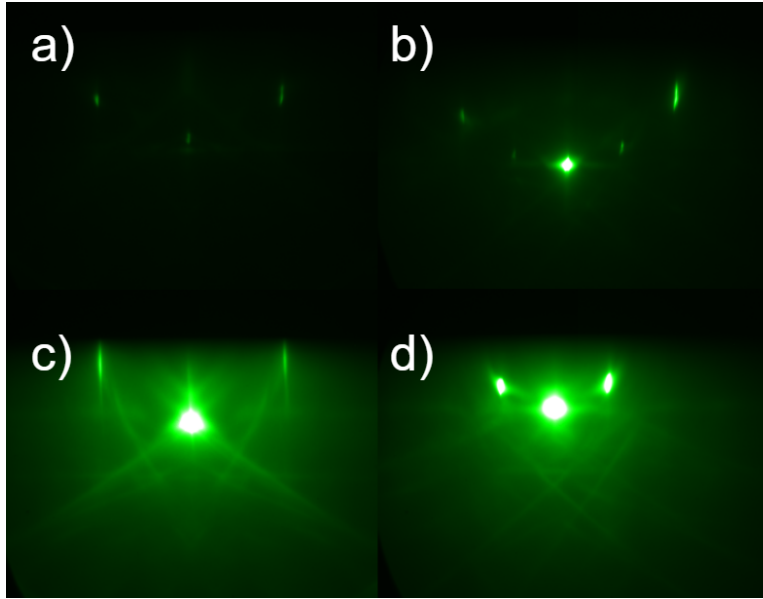


Figure 3.7: RHEED images of the sapphire surface along the two crystallographic directions where a) and c) belong to the $[10\bar{1}0]$ direction and b), d) belong to the $[11\bar{2}0]$ direction. Top sub-figures are pre-annealed substrates and the bottom sub-figures are post-annealed RHEED images. Note: the RHEED intensity dramatically increases after annealing at high temperature. .

Codeposition vs Shutter Growth

When growing materials, there are often two grow approaches: to grow using a codeposition or to grow using a shutter method. Codeposition refers to when all elements are simultaneously deposited and shutter growth is a deposition method in which each element is deposited individually. In the codeposition method, it may be hard to control the type of growth mechanism. If there is no self assembly of the crystal structure, it is possible to have a mess of elements with the correct stoichiometry form multiple

3.1. Sapphire FGT growth

phases. This is further complicated when involving materials with high vapor pressure, as it is not necessarily safe to assume the sticking coefficient of elements or compounds (the relative number of atoms deposited as compared to the number of atoms which strike the surface) while depositing at high temperature, because of their temperature dependence [49]. In practice, it is not straightforward to determine the stoichiometry. Another difficulty arises when having to calibrate fluxes of each elements to agree within a few seconds. Each flux calibration averages roughly 30 minutes. Thus, tuning the deposition rates precisely can be a multiple hour task.

On the other hand, in the shutter method, it may be hard for elements to find their home and have the proper mobility, as each element is deposited at cooler temperatures as a way to control the SC. One also has to navigate unwanted phases growing before all elements have been introduced, especially when there are 3 unique elements all being epitaxially delivered.

In the early trials, codeposition was the method of choice. Fe, Ge and Te fluxes were measured with a quartz crystal monitor (QCM) and stoichiometrically calibrated. Fe, Ge and Te deposition rates were set such that a single layer or half unit cell of FGT was to be delivered to the substrates surface over a period of 580 seconds. The substrate temperature was held at 340°C, the Fe, Ge and Te crucibles were held at 1120, 997, and 315 °C respectively. After 3 layers(1.5 unit cells) the substrate RHEED pattern was no longer visible and the new surface had significantly less RHEED intensity, almost appearing amorphous as displayed in Figure 3.8.

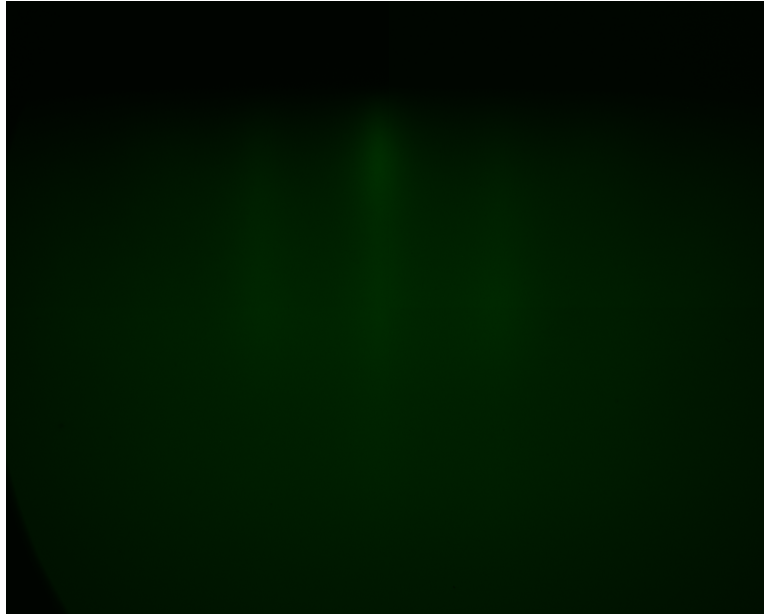


Figure 3.8: RHEED image of the first attempt at growth of FGT using the codeposition method on the sapphire surface. Three streaks are faintly visible. In-plane lattice parameters were extracted to be roughly 4\AA . Note: the lack of general intensity is due to a low RHEED emission current and significant amount of diffuse scattering.

3.1. Sapphire FGT growth

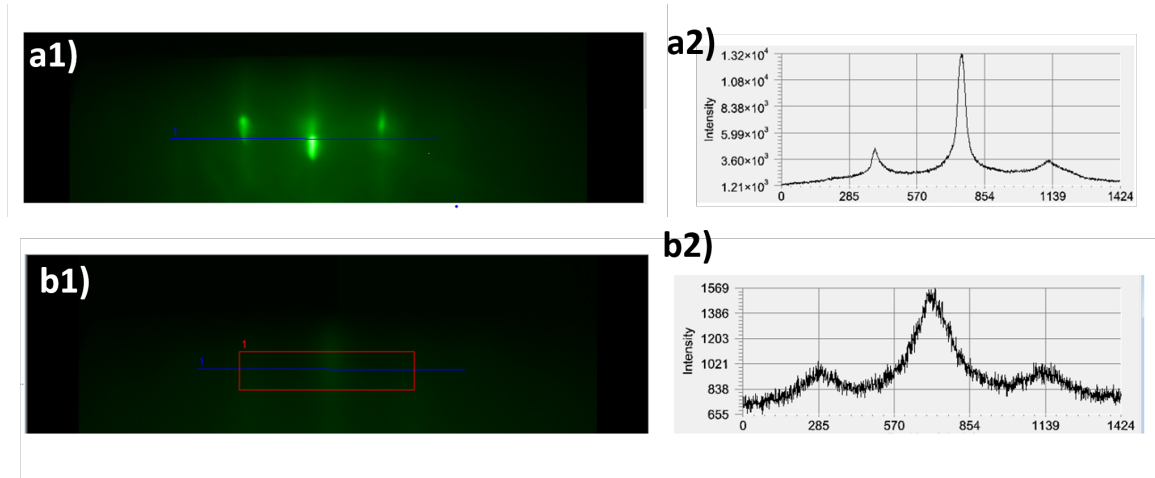


Figure 3.9: Line profiles of a) sapphire substrates and b) possible films. Left: RHEED images of the grown film's $[11\bar{2}0]$ direction. Right: corresponding line profiles of the diffraction pattern. Lattice constants are extracted using the ratio of the pixel peak positions. Note: the poor intensity in b1) is likely due to disorder and low emission current.

A line profile was taken of the two RHEED directions of Figure 3.8 and used to determine the in-plane lattice constants of what was grown. Upon investigation, the in-plane lattice parameters agreed well with those of FGT. The theoretical mismatch was calculated to be 15.7% and the experimental mismatch was found to be 15.8%. This film was grown only a few layers so it did not permit for further diffraction experiments like XRD, but yielded promising in-plane lattice parameters as detailed in Figure 3.9

Future attempts at the growth of FGT were performed with the shutter method, in which subsequent layers of Te, Fe, FeGe, Fe and Te were deposited in that order. Each layer was deposited at 200 °C. with the same substrate preparation as described above. Early attempts resulted in polycrystalline films as shown in Figure 3.10 where the circular diffraction rings indicate no preferred orientation of the crystal.

To gain more information on the grown materials, lattice constants both in- and out- of plane were analyzed using line profiles as displayed in Figure 3.11. In this sample, a Fe:Ge:Te stoichiometry of 2.7:1:2 was used. The Fe ratio was chosen such that no excess Fe was deposited, but still within the window of stable FGT Fe concentration [24]. The Te flux was chosen to match that of bulk crystal growths. The film did not display a change in

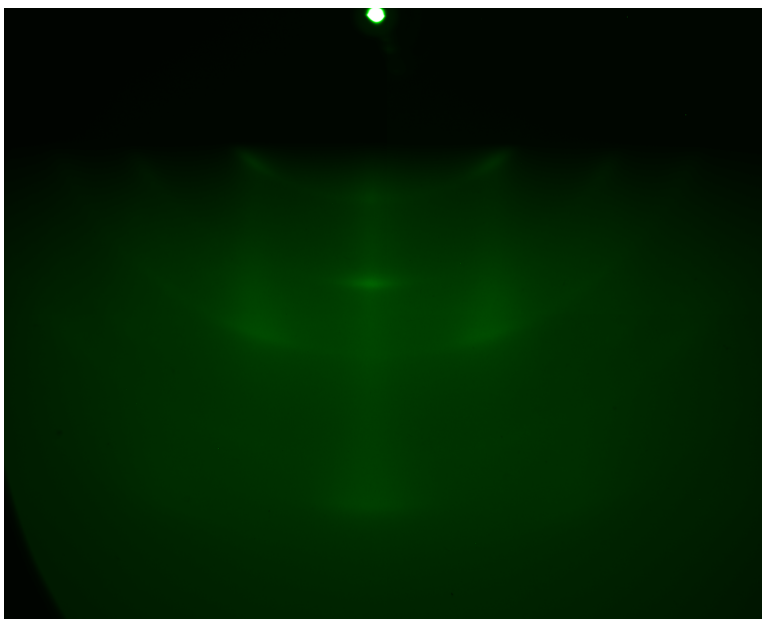


Figure 3.10: RHEED images of a polycrystalline film grown on the sapphire (0001) surface. Polycrystallinity is inferred from the diffraction rings.

RHEED upon rotation of the sample indicating no preferred orientation of the film. The film also displayed polycrystalline rings. This made it impossible to determine the crystal symmetry. Yet, by analyzing line profiles of the RHEED images, it was possible to determine in-plane lattice constants. The lines are displayed in Figure 3.11 a1) and b1) by the thin lines. The lattice constants were analyzed by the distances between peak as indicated by the black lines in all sub-figures. The in-plane constant was determined to be 3.66 Å and the c lattice constant was determined to be roughly 8.3 Å which are in disagreement with expected FGT lattice parameters.

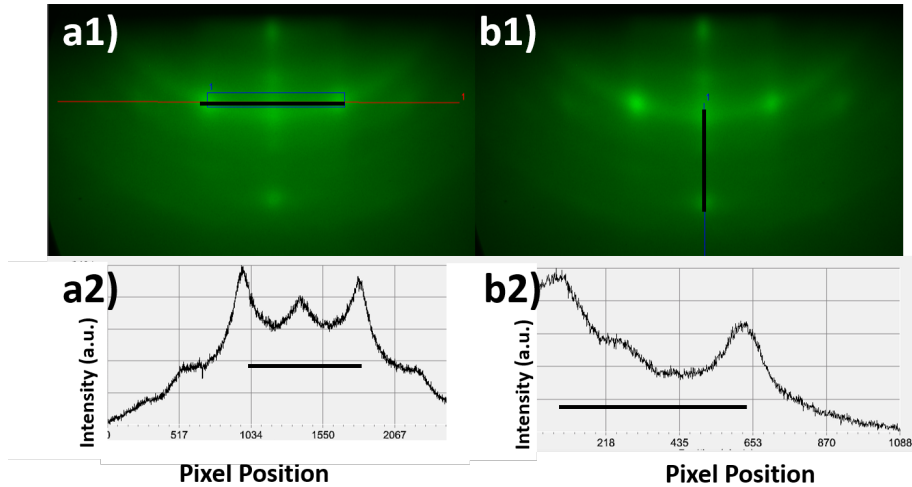


Figure 3.11: RHEED image of polycrystalline sample with 3D character. Line profiles of both the in-plane and out-of-plane lattice constants are displayed in a and b respectively. The c lattice constant was determined to be 8.3 \AA . The in-plane lattice constant was determined to be 3.66 \AA . These samples were grown with a 2 x over flux of Te atoms.

Further attempts were made by changing the Te flux ratio. SC's were assumed to range anywhere between 0.75 to 0.5 as displayed in Figure 3.12. Each film resulted in a polycrystalline, three-dimensional diffraction pattern. The diffraction pattern of each sample did not change upon rotation. This indicates that the films were grown such that the film did not have a preferred orientation. Films with less tellurium tended to be more polycrystalline while films with more tellurium tended to have a preferred orientation. Experiments to determine a more accurate tellurium SC were then carried out. Samples were grown at 280°C with up to 2 x Te overflux with corresponding data displayed in Figure 3.12. This experiment highlights the necessary Te overflux required in the growth of FGT. As the Te flux is increased the film began to become less polycrystalline and 3D. Once the tellurium SC had been assumed to be 0.5 growths were more controllable. At this point the substrate temperature was varied to find the optimal deposition temperature with little success. Thicker films of 20 layers were grown and diffraction experiments were carried out and are recreated in Figure 3.13

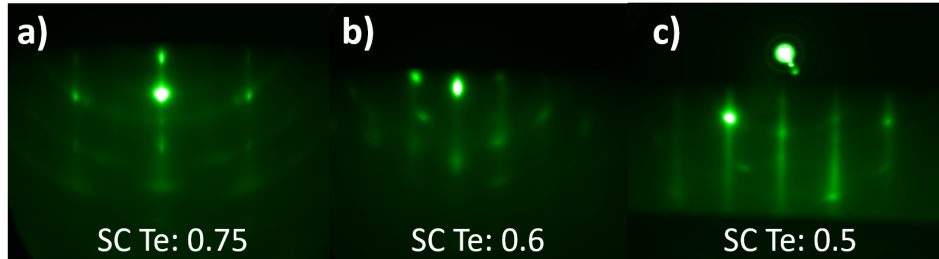


Figure 3.12: Examples of RHEED images with varying amounts of Te flux in codeposition growth. Substrate temperature was held at 300C. a) the SC is assumed to be 0.75 thus 3 of every 4 atoms were assumed to stick to the film surface. The surface appear very three dimensional and slightly polycrystalline. b) SC's assumed to be 0.6 resulting in a less polycrystalline sample but still 3 dimensional. c) 2 dimensional streaks are visible with a some 3 dimensional spots. All emission current was measured at $0.2\mu A$

In codeposition growths at 300°C the diffraction patterns began to change as the samples were rotated indicating at least a preferred film orientation. The RHEED appeared streaky indicating smooth surfaces, and the in-plane lattice constants were in agreement with FGT. Yet the films RHEED showed that the growth was still not perfected. The existence of a double streak marked with blue stars at what was assumed to be the 2nd order diffraction streak indicated either multiple phases (the existence of what could be the (10) diffraction peak of FeTe, or a double domains $[11\bar{2}0]$ direction overlap with the $[10\bar{1}0]$ direction). Diffraction experiments revealed there were multiple phases of FeGe compounds, but also the existence of FGT. Further trials of the growth of FGT on sapphire were unsuccessful.

3.2 Ge FGT growth

Codeposition vs Shutter Growth

Due to the difficulties of growth on the Al_2O_3 surface, a different substrate was used. Ge (111) was chosen due to its matched in-plane lattice symmetry as well as its similar in-plane lattice constants of 4.013 \AA resulting in a 0.5% lattice mismatch. This substrate also granted us the ability to deposit a Ge wetting layer on the Ge surface to ensure atomic smoothness as well as bury

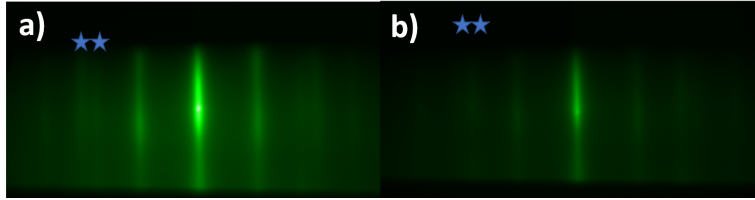


Figure 3.13: First truly 2 dimensional RHEED images obtained during shutter growth on sapphire. a) and b) were taken upon 30 degree rotation which would reveal the two unique crystallographic directions. The RHEED profile did not change upon 30 degree rotations indicating a film with no preferred orientation. Double streaks were also observed at the 2nd order diffraction points which indicated either multiple phases of Fe, Ge compounds or the incident beam probed areas with different FGT orientation. RHEED emission current was measured to be $0.3 \mu\text{A}$ upon each image taken. These films were determined to be significantly Te deficient.

any contaminants that may exist on the substrate surface after placement into the MBE chamber.

Like many substrates, Ge is prone to surface contamination. In particular, a native oxide is known to form on the surface of Ge(111). Furthermore, organic contaminants likely reside on the sample surface which are not easily removed. Thus an etching procedure was developed to rid the substrate surface of organic compounds and remove the surface oxide layer.

Delivered samples were subject to a “piranha etching” procedure to remove the organic compounds. This involved a mix of 1:3 solution of hydrogen peroxide (H_2O_2) to sulfuric acid (H_2SO_4). It is important to note hydrogen peroxide was added after sulfuric acid for safety reasons. The solution was then heated to 130°C on a hotplate while stirred. It was soon realized that this process was very time sensitive. Substrates left in the solution for too long would develop a unidentified milky haze on the surface which was not removable, thus rendering the substrates useless. Optimal time in the piranha etch was determined to be roughly 30 seconds while on the hotplate. The substrates were subsequently placed in deionized water (DI), then added to a second solution of 23:1 DI water to hydrofluoric acid (HF) for 30 seconds. Samples were again placed in DI water until loaded into the chamber. Substrates were finally degassed in the MBE chamber. Temperatures were ramped at $20^\circ\text{C}/\text{min}$ to 480°C while maintaining chamber pressures below 5×10^{-9} torr. Upon approach to 480°C the Ge(111) surface obtained a

3.2. Ge FGT growth

2×2 reconstruction. The reconstruction did not survive temperatures much larger than 480 but were robust while cooling. Once the reconstruction was obtained, two additional monolayers of Ge were deposited or for as long as the RHEED intensity increased.

Examples of the substrate at 200°C and at 480°C are displayed in Figure 3.14. These images were taken in the two unique crystallographic directions namely the $[10\bar{1}0]$ and the $[11\bar{2}0]$ directions labeled a) and b) respectively. At 200°C the Ge surface does appear crystalline but the RHEED intensity is largely diffuse. This is likely due to residual surface contamination developed while transferring the substrate from the DI to the chamber. The intensity of the spectral and higher order diffraction spots observed in the higher temperature images a2) and b2) are indicative of a highly ordered atomically smooth surface. The less intense spots located between the bright spots are characteristic of a 2×2 reconstruction. After the reconstruction, substrates were placed in a diffractometer to determine the exact position of Ge peaks.

XRD was performed in a Rigaku Smartlab system at room temperature. A parallel beam (PB) configuration was implemented with a copper anode where both $K\alpha 1$ and $K\alpha 2$ emission channels were used. The voltage and current were set to 40 kV and 44 mA, respectively.

A Ge sample was first inserted into the instrument to note the peaks belonging to the substrate. A 2θ - ω scan is displayed in Figure 3.2. The (111) and (333) peaks are most prominent at 27 and 90 degrees respectively. The (311) peak is also observed at roughly 57 degrees. the (111) peak corresponds to a lattice spacing of 3.27 Å.

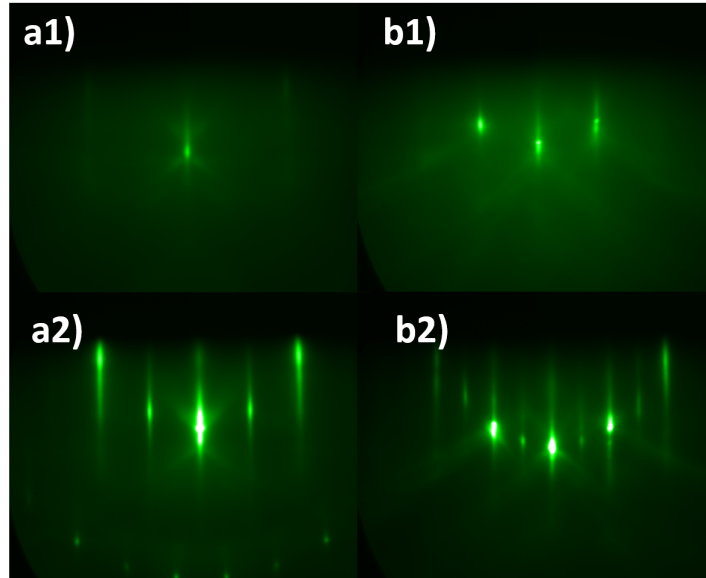


Figure 3.14: RHEED images of Ge samples in the two unique crystallographic directions. a) and b) are Ge samples in the $10\bar{1}0$ and $[11\bar{2}0]$ directions respectively. a1) and b1) are taken at low temperature (200°C) while a2) and b2) are taken at 480°C . The streaks not visible in a1) and b1) are indicative of a reconstruction, more specifically since the half order streaks are observed in both crystallographic directions the reconstruction is determined to be 2×2 .

Like the sapphire substrates, both shutter and codeposition methods were performed with varying degree of success. Shutter method growths were attempted with substrates held at room temperature. The Fe, Ge and Te cell temperatures (deposition times) were held at $1180(240\text{s})$, $1070(130\text{s})$ and $320(117\text{s})$ $^\circ\text{C}$ respectively. Because the QCM calibrations were performed at room temperature, the Te SC with respect to QCM was determined to be 1. This was a major factor in deciding to deposit at room temperature. The shutter growth method was performed layer by layer according the structure of the material thus stoichiometric ratios of Te, Fe, FeGe, Fe, Te layers were deposited subsequently. Corresponding RHEED images are pictures in Figure 3.16, where a 10 unit cell (UC) film is pictured. The sample appears single phase in the RHEED images with in-plane lattice constants corresponding to 4 \AA with no polycrystallinity.

3.2. Ge FGT growth

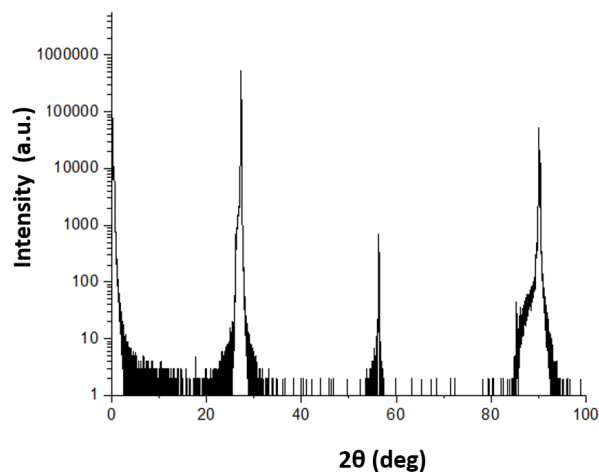


Figure 3.15: 2θ - ω scan from 0-100 deg. of the Ge(111) surface. Note there are three main peaks at 27, 90 and 57. Those at 27 and 90 deg are the Ge (111) and (333) peaks respectively corresponding to a lattice spacing of 3.27 Å. The less intense peak at roughly 57 deg. belongs to the (311) diffraction plane.

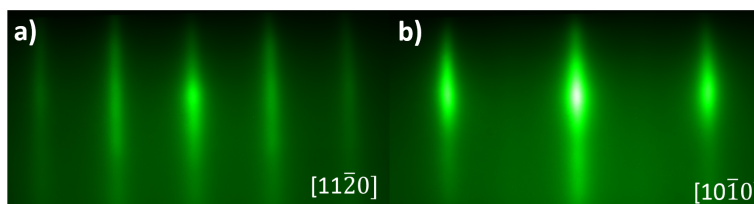


Figure 3.16: RHEED images of FGT shutter method of 10 UC of FGT and other phases. a) RHEED beam aligned with the $[11\bar{2}0]$ direction and b) RHEED beam aligned with the $[10\bar{1}0]$ direction. The RHEED emission current was held at $0.3\mu A$

Diffraction measurements were then attempted to determine the c lattice parameters of the film and to identify any other phases that may have existed. The diffraction scan is shown in Figure 3.17.

The scan was performed from 0 to 90 degrees in air at room temperature.

3.2. Ge FGT growth

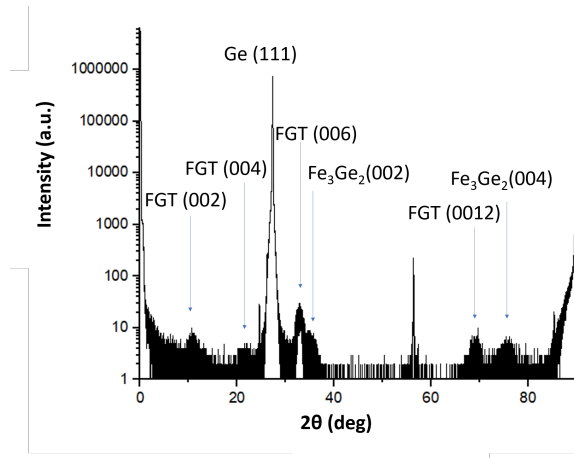


Figure 3.17: XRD 2θ - ω scan from 0-90 degrees of shutter growth method of a 10 UC film on Ge (111). The sample has multiple Te deficient phases such as Fe_3Ge_2 . Yet there are signs of FGT as indicated by the FGT labeled peaks.

The sample was found to contain multiple phases, namely FGT and FGT. This was a sign that the corresponding film was Te deficient. The most pronounced peak is the Ge (111) peak. This is due to the thickness of the substrate. The (0 0 2n) peaks of Fe_3GeTe_2 are observed indicating progress at the growth of single phase FGT. There are also other phases observed in the scan namely the Fe_3Ge_2 phase.

AFM experiments were then carried out to analyze the topography of the sample. At this point the effects of exposure to oxygen were still not well known. Nevertheless, AFM scans were taken revealing a very rough surface as displayed in Figure 3.18. The height variation over the $2 \times 2 \mu\text{m}$ scan was as large as 17 nm. This was a sign that growth at higher temperature could be necessary. The increased growth temperature could in theory lead to better film quality because of the increased mobility of exptaxially delivered atoms, but also alter the Te sticking coefficient.

Once some FGT phase was confirmed, it was then possible to perform transport measurements to probe for magnetic order. The R_{xy} scan of a 10 UC FGT film grown by shutter growth is recreated in Figure 3.19. At low temperatures (2, 50 K) hysteresis are observed implying ferromagnetic order at low temperature. The transport data revealed that the FGT phase yield

3.2. Ge FGT growth

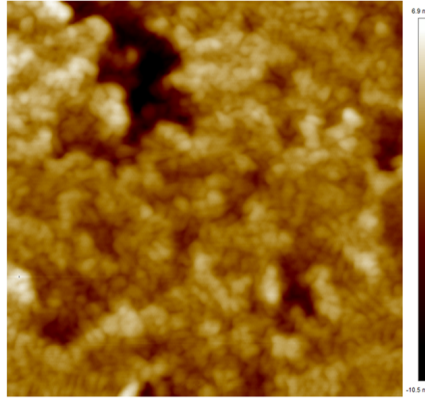


Figure 3.18: $2 \times 2 \mu\text{m}$ AFM image of a 10 UC FGT surface grown on Ge(111). Sample was grown using the codeposition method. The surface appears quite rough. Height variations over the scan are as large as 17 nm. Later experiments would further complicate analysis since the FGT surface is highly sensitive to ambient conditions. This sample was exposed to such conditions for multiple hours.

a signal despite the existence of other phases. The FGT phase responsible for the data must have existed across the entire substrate.

Following the shutter method growths resulting in rough surfaces, the codeposition method was attempted at higher substrate temperatures with parameters as follows. An Fe:Ge:Te: stoichiometry of 2:1:4 was used with a monolayer growth period of 240 s, and Substrates were held at 320 °C. After deposition of 4 layers substrates were annealed to 340 C for 1 hour. This process was repeated until 10 UC had been deposited just as in the shutter growth process. As displayed in Figure 3.20 the growth led to a surface which was two dimensional as indicated by the streaks nature of the RHEED intensity. In Figure 3.20 a) and b) correspond to the two unique diffraction directions namely the $[11\bar{2}0]$ and $[10\bar{1}0]$ directions respectively. The emission current held at 0.2 μA for both pictures. In either direction no secondary phases or polycrystallinity was observed. This was a promising result, as no single phase codeposition had been observed in sapphire growths. The sample was then fully characterized with XRD, AFM and transport.

In the diffraction experiment, the sample revealed multiple peaks corresponding to materials other than FGT. The same Fe_3GeTe_2 peaks were observed as in the shutter growth sample. But the relative intensity of these

3.2. Ge FGT growth

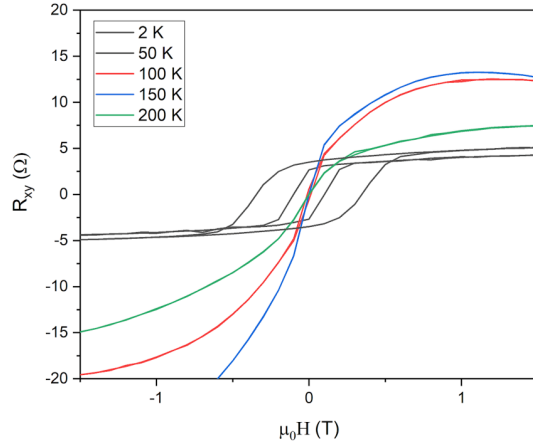


Figure 3.19: Transport data of FGT shutter method of 10 UC of FGT and other phases. Data was taken in a Quantum Designs PPMS. Out-of-plane magnetic fields were swept from -3 to +3 T at temperatures ranging from 2 to 200 K. The closure of the hysteresis loop implies a transition from the ferromagnetic to paramagnetic state at 50 K.

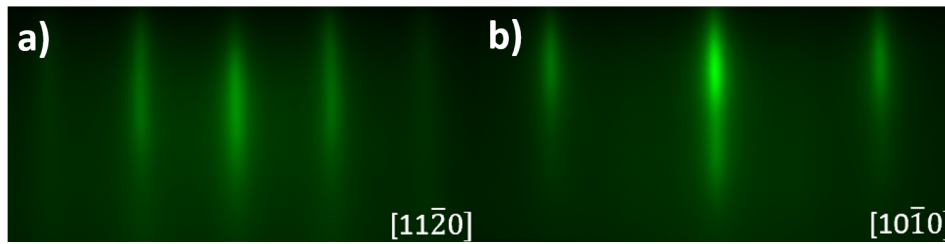


Figure 3.20: RHEED images of FGT co-deposition method of 2 UC of FGT and other phases. a) RHEED beam aligned with the $[11\bar{2}0]$ direction and b) RHEED beam aligned with the $[10\bar{1}0]$ direction. The RHEED emission current was held at $0.2 \mu\text{A}$

peaks relative to that of shutter growth was much less. But, like shutter growth, the codeposition recipe was still Te deficient.

Following in-situ characterization the film was taken the AFM in order

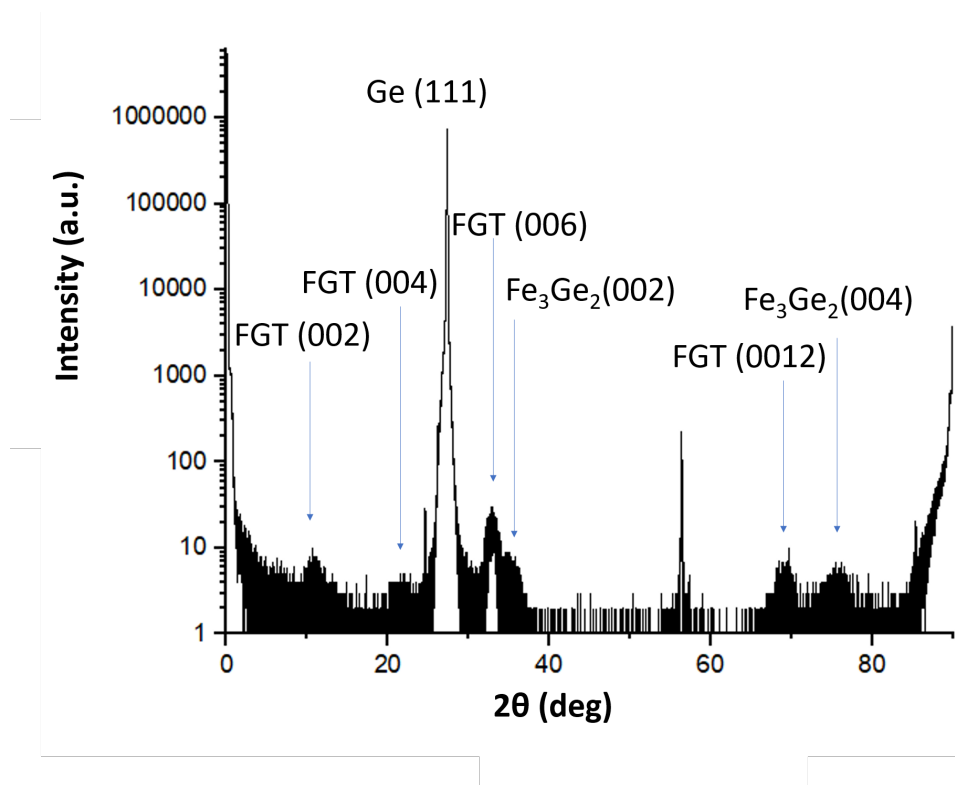


Figure 3.21: 2θ - ω scan of a 10 UC co-deposited FGT film on Ge(111). The data reveals a mixed phase film with numerous diffraction peaks. Those belonging to FGT and Fe_3Ge_2 are labeled.

to examine its typography, particularly the smoothness of the surface. The resulting $2 \times 2 \mu\text{m}$ scan of the surface is displayed in Figure 3.22. The vertical range recorded was roughly 2.5 nm over the entire scan range implying uniformity over the substrate surface. Upon comparison to the shutter growth method, the surface was an order of magnitude smoother yet it was still not atomically smooth. The lack of atomic smoothness could be from a rough substrate surface, poor growth technique or oxidation of the surface upon exposure to air. The substrate and film surface imply atomically smooth surfaces in RHEED, thus we were led to believe that the surface exposure to air was responsible.

Transverse transport measurements on the sample were carried out from

3.3. Capping Decapping

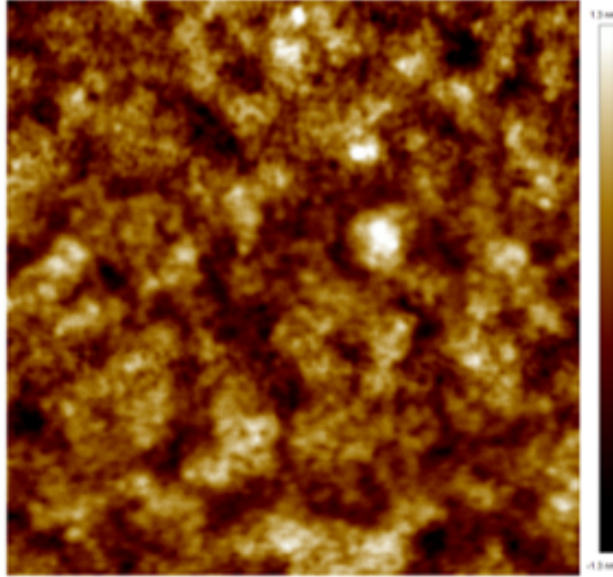


Figure 3.22: $2 \times 2 \mu\text{m}$ AFM image of the FGT surface grown on Ge(111). Sample was grown using the shutter method. Over the scanned area, height variation up to 2.4 nm was recorded

2 to 250 K subject to magnetic fields ranging from -3 to +3 T. The corresponding data is displayed in Figure 3.23. The co-deposited sample shows an anomalous Hall response up to 250K. FM order indicated by a hysteresis loop halts at roughly 150K as indicated by the closure of the hysteresis.

It was concluded from these experiments that the most promising approach synthesizing atomically smooth single phase FGT was the codeposition method.

3.3 Capping Decapping

After previous reports suggesting samples were air sensitive [50], a capping procedure was necessary to measure thin (few QL) samples. The capping material needed to be removable at low temperatures. More specifically, the cap needed to be removable at temperatures lower than the growth temperature of the films in order to avoid sample degradation. Additional

3.3. Capping Decapping

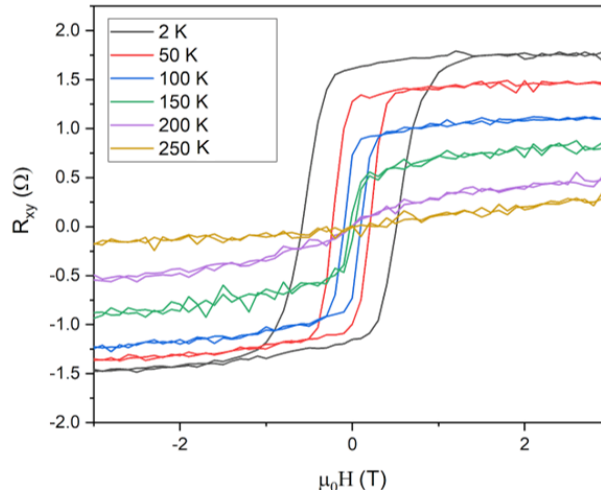


Figure 3.23: Transport data of 10 UC FGT grown via codeposition with other phases. Out-of-plane magnetic fields were swept from -3 to +3 T at temperatures ranging from 2 to 250 K. The closure of the hysteresis loop implies a transition from the FM to paramagnetic state at roughly 150 K.

restrictions were imposed by the possibility of intermixing at the sample/cap interface. If the cap and the Te layer share the same valence states and are similar in ionic radii, it is likely that substitution would take place at the interface. Because there existed no way to check for such substitution at UBC, it was in our best interest to stay away from materials which this was possible.

Ideally, the sample cap would also be amorphous to best protect the sample, as domain boundaries and other crystal defects invite oxidation and contamination through such defects. Many of the elements available in GM2 were out of the question. For example, Fe and Ge would almost certainly be irremovable due to their low volatility at low temperature. Compound caps grown with multiple elements were a possibility, but all compounds available such as GeTe and FeGe yielded lower vapor pressures than some individual elements alone. At our disposal there existed two elemental candidates, namely Te and Se, which could serve to cap. Se has a higher vapor pressure than Te and its volatility makes it easier to remove. Yet with Se deposition we risk Se substitution at the surface/interface. Although this substitution may only be minor in monolayer and few layer experiments, these substitutions may have dramatic effects especially when the Te is responsible for

3.3. Capping Decapping

many of the interesting physical phenomena that make FGT so attractive through means of spin orbit coupling.

Te on the other hand also has a relatively high vapor pressure and any intermixing of the cap and film was nothing to fret. Capping experiments were carried out with Se and Te. First Te was attempted at room temperature as displayed in Figure 3.24 where a) is the diffraction pattern of a highly ordered monolayer FGT sample which is indicated by the point-like diffraction. In b, a 20nm Te cap is displayed. During the capping proce-

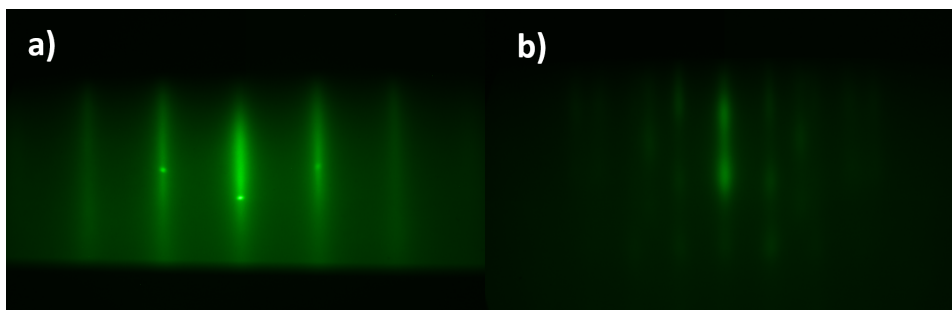


Figure 3.24: RHEED images of FGT film and cap. a) The RHEED profile of FGT film along the $[11\bar{2}0]$ direction with point-like diffraction spots signaling a well ordered atomically smooth film. b) Te cap indicating 3D surface defects.

dure the Te cell was held at 320°C for 30 minutes. The film was held at room temperature. The resulting cap was initially amorphous, but during the growth become crystalline and slightly 3D as indicated by the spotty and streaky nature of b). Decapping of the sample was then attempted. The sample was heated from room temperature at a $5^{\circ}\text{C}/\text{min}$ ramp rate. At 250°C the sample was held for 30 minutes with no change in RHEED. After 30 minutes the sample was heated to 280°C with a $1^{\circ}\text{C}/\text{minute}$ ramp rate. At this point the cap started to decompose, and annealing was held at 280°C , the surface was left resembling that of FGT as displayed in Figure 3.25. The resulting RHEED intensity along the $[11\bar{2}0]$ direction was largely diminished with a significant amount of diffuse scattering. The in-plane lattice constants were similar to those of the original film. The sample was then removed from the chamber where diffraction measurements were performed in the usual manner. The XRD scan revealed no FGT phases left therefore indicating that the decapping process was detrimental to the FGT film. This was interesting because the sample was never raised above

3.3. Capping Decapping

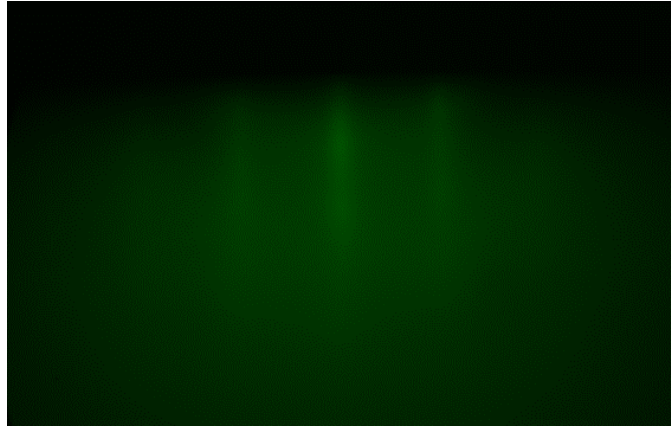


Figure 3.25: RHEED image of film post Te decapping experiments. The diffraction pattern slightly resembles the $[11\bar{2}0]$ direction of FGT. Emission current is held at $0.2 \mu\text{A}$. Note: the blur seen in the image is due to an increase amount of diffuse scattering due to a imperfect surface.

the growth temperature during the decapping process.

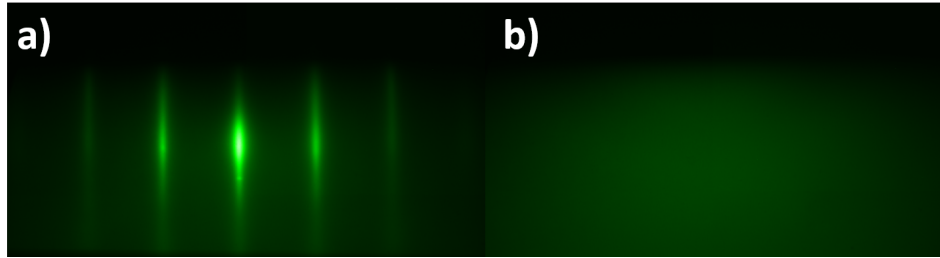


Figure 3.26: RHEED images of a) 2 UC FGT sample and b) amorphous Se cap.

After the failed Te capping process a Se cap was attempted. The same thickness of cap (20nm) was deposited on on a 10 QL FGT sample as displayed in Figure 3.26. The crystal quality of the film was very good, with point-like diffraction and a negligible amount of diffuse scattering. The Se cap also grew quite well. The resulting cap was completely amorphous as indicated by the lack of any concentrated intensity in the image. The decapping process was attempted in a similar fashion to the Te cap, but the

3.3. Capping Decapping

ramp rate differed slightly. The Se decapping process was started at room temperature and was then heated at 2° per minute to 250°C where the RHEED intensity began to change. Initially a diffraction pattern resembling FGT was observed but with a 2×1 reconstruction as displayed in Figure 3.27.

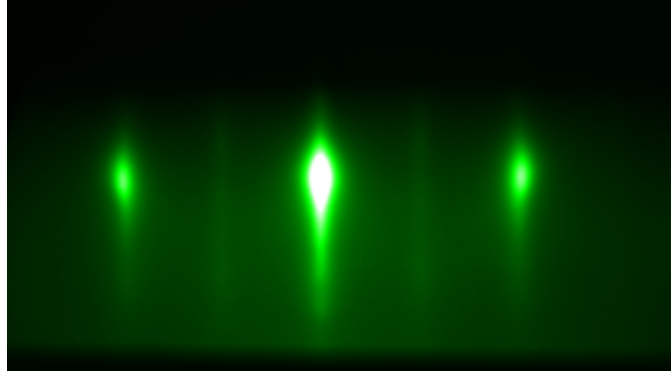


Figure 3.27: RHEED image of a film surface during the decapping procedure. the surface shows signs of a 2×1 reconstruction as indicated by the faint half order streaks.

After 10 minutes at 250°C the sample began to become 3D, and wors-

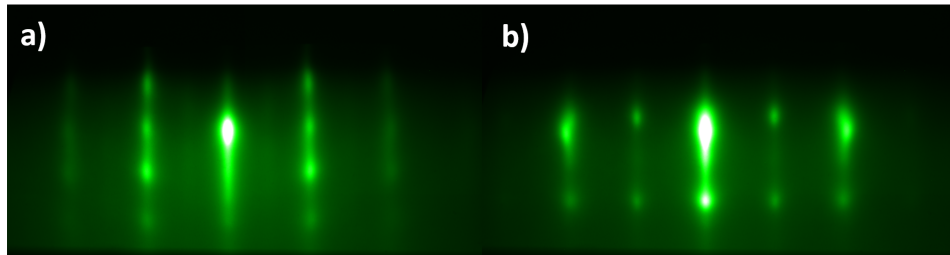


Figure 3.28: RHEED images of the Se decapped FGT films. The two unique crystallographic directions both exhibit 3D surfaces with what appears to be a slight 2×2 reconstruction. The reconstruction was not removable under any conditions which conserved the underlying film. Thus proving Se was not an ideal candidate for capping/decapping procedures.

ened quickly. The symmetry of the crystal remained 3 fold and the two crystallographic directions are shown in Figure 3.28. Interestingly, the c

3.3. *Capping Decapping*

axis parameter was not shared between the two directions which is illustrated by the intensity modulations following a specific streak vertically. Due to the obvious degradation of the sample no further characterization measurements were performed. From these experiments the hopes of successful decapping procedures were abandoned. This implied that any surface sensitive measurements were required to be performed in-situ to avoid exposure to the atmosphere. Once a cap was deposited the cap would need to remain on the sample surface to ensure pristine films. It then implies that the techniques like scanning tunneling microscopy and angle resolved photoemission spectroscopy would be out of the realm of possibilities unless such apparatuses were to be directly connected to the system or a vacuum suitcase was used.

Chapter 4

Experimental results

4.1 Structural Characterization of Pristine FGT Samples by Co-Deposition

In early experiments co-deposition seemed to be the most promising route as indicated by transport and diffraction measurements, thus the substrate temperature and Te over flux parameter space was explored. Growth above 360°C was found to decompose FGT phases, and growth below 280°C led to FeTe phases as indicated by diffraction measurements. Sample growth temperatures were chosen to be 330°C at which Te overflux was optimized at 320% where up to 400% Te flux did not change the growth, thus one could assume that the constant deposition was in equilibrium with evaporation at the sample surface. Higher than 400% excess Te was shown to decrease the RHEED intensity such that the evaporation rate could not match that of the deposition rate.

Source materials of Fe, Ge, and Te were evaporated from the effusion cells at 1320°C, 1100°C, and 325°C, respectively. Elements were co-deposited on the substrate at 330°C to grow FGT. The ratio of Fe:Ge:Te was set at 3:1:5.6 measured by QCM prior to growth. These temperatures and flux ratios were determined to yield optimal FGT films. It was then possible to grow optimized high-quality growth of epitaxial FGT(0001) ultra-thin films with thicknesses ranging from 1 QL to 10 QL on atomically smooth Ge(111) substrates. Corresponding FGT RHEED images are displayed in Figure 4.1. a) and b) are the usual Ge surfaces where the 2x2 reconstruction is apparent as displayed by the half order streaks. c) and d) are images of a 4 QL FGT surface where point-like diffraction spots are indicative of well ordered atomically smooth surfaces. Both crystallographic directions are displayed in Figure 4.1 in which a hexagonal lattice directions, to which FGT and Ge(111) belong, there exist two distinct crystallographic directions separated by 30 degrees, the $[11\bar{2}0]$ and $[10\bar{1}0]$ directions. In-plane lattice parameters are measured in-situ throughout the growth process using RHEED line intensity profiles of the associated diffraction patterns. The

4.1. Structural Characterization of Pristine FGT Samples by Co-Deposition

lattice constant of the FGT film 3.99 Å agrees with the known in-plane lattice constant for bulk Ge(111), as well as the bulk FGT measurements [32]. It is essential to note the diffraction patterns of the two crystallographic directions of the substrate and film are aligned, which confirms an epitaxial growth as displayed in Figure 4.1.

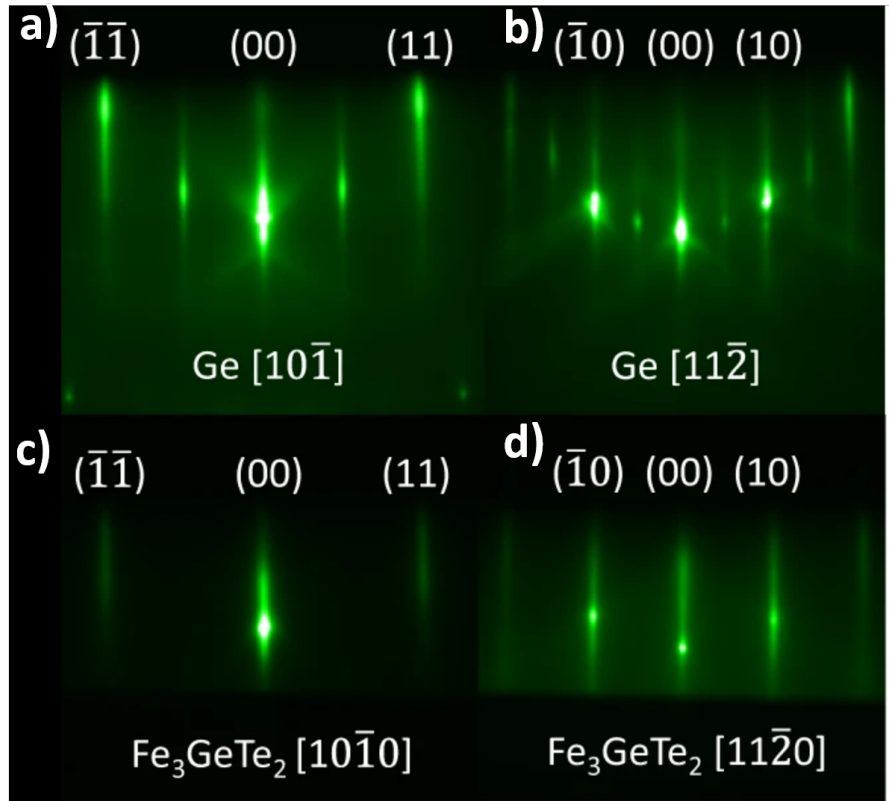


Figure 4.1: In-situ RHEED images of a 22 reconstructed Ge (111) substrates along the $[10\bar{1}0]$ and $[11\bar{2}0]$ direction. Bottom: 4-QL Fe_3GeTe_2 with electron beam along $[10\bar{1}0]$ direction and $[11\bar{2}0]$ direction.

A layer-by-layer growth mode is established via observation of RHEED intensity oscillations as displayed in Figure 4.2. The oscillation period allows the precise control of the number of layers deposited in thick samples as well as determines the exact amount of time-per-layer to minimize layer number

4.1. Structural Characterization of Pristine FGT Samples by Co-Deposition

differences within a sample. The oscillation period was determined to be 78 seconds which was highly reproducible. In thinner samples a calibration sample was used to determine the layer oscillation period such that shutters could be closed before the downturn in the intensity and correspondingly the next layer began to form was observed. In this experiment the 1st diffracted (01) and specular spot (00) in Figure 4.1 oscillations were in-phase, and the oscillations began at a maximum thus we could conclude that a downturn in the intensity indicated the start of a new layer.

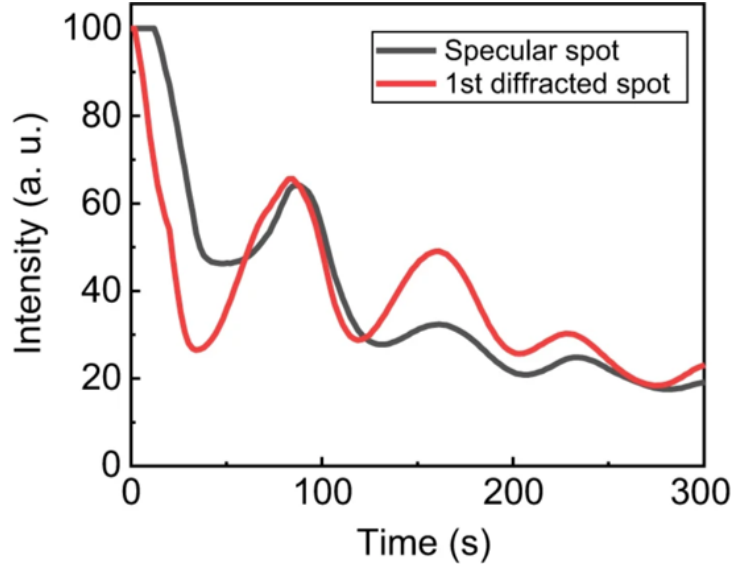


Figure 4.2: RHEED intensity oscillations during the growth of Fe_3GeTe_2 , indicating atomic smoothness and its epitaxial growth mode. Single QL growth times are extracted from the period of oscillation to be 80 s.

The lattice structure of FGT films were further characterized by ex-situ XRD. A single phase of FGT (001) films is confirmed by the (002) family of diffraction peaks in Figure 4.3. The diffraction pattern suggests a out-of-plane lattice constant $c=16.355 \text{ \AA}$, in good agreement with bulk measurements of 16.33\AA [32]. Fe vacancies in the Fe^{2+} site have been shown to decrease in-plane lattice constants and increase c [51], which are not observed in our films. Experiments were performed to conclude if the FGT surface is air sensitive as no previous reports of FGT did detail capping procedures[24], while also stating fabrication had been done in oxygen free environments. A 10 QL FGT sample was removed from the MBE cham-

4.1. Structural Characterization of Pristine FGT Samples by Co-Deposition

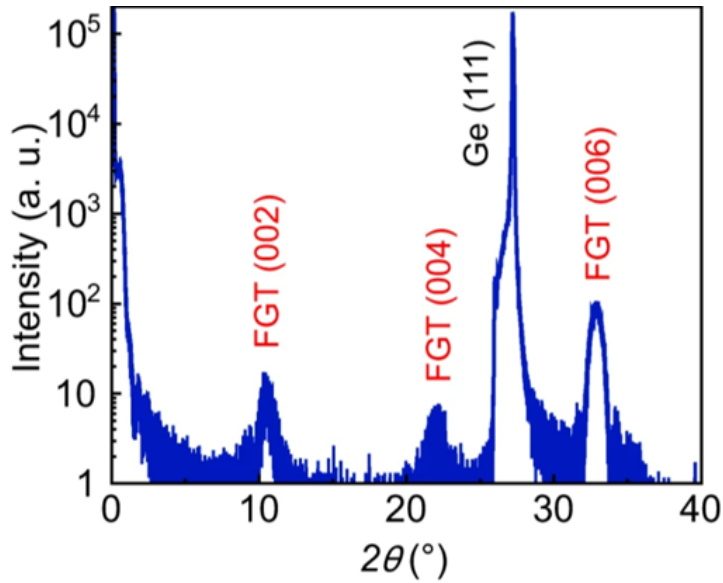


Figure 4.3: Ex-situ XRD of the out-of-plane lattice structure of FGT films. A single phase of FGT (001) films is confirmed by the (002) family of diffraction peaks. The diffraction pattern suggests a out-of-plane lattice constant $c = 16.355 \text{ \AA}$, in good agreement with bulk measurements of 16.33 \AA . The shape of peaks has been observed for all samples of pure FGT, the odd shape of such peaks could be due to thin samples unable to generate significant peaks or large scan speeds.

ber and exposed to ambient conditions for a few hours. Once placed back into the chamber the surface had become completely amorphous indicating no crystalline structure (amorphous) remained after exposure to ambient conditions. Upon placement in the chamber, the sample was slowly heated (softly baked) to 340°C in at a rate of 2 deg/min while chamber pressures were kept below $5 \times 10^{-9} \text{ torr}$. The surface did not recover in any soft bake experiments. An example of such a surface is displayed in Figure 4.4

4.2. *Transport results showing the conductivity and ferromagnetism in Fe_3GeTe_2 films*

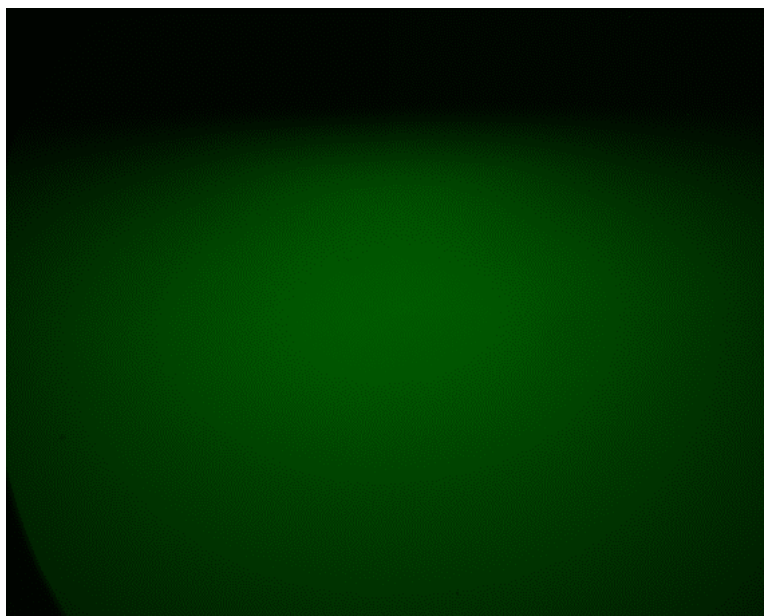


Figure 4.4: Diffuse scattering FGT sample after exposure to ambient conditions for only a few minutes. The lack of features revealed by the RHEED image implies an oxidized amorphous surface. This is hard evidence that the surface layers of FGT are air sensitive. The amorphous layers were not removable after soft bakes up to 340C. This also served as an indication that any AFM scans are not of the FGT surface but of an oxidized surface that may not reflect the surface smoothness of the film in the chamber.

4.2 Transport results showing the conductivity and ferromagnetism in Fe_3GeTe_2 films

After fully characterizing the structure, single phase single domain FGT films could be measured in a PPMS, where electronic and magnetic properties of FGT films were characterized by transport measurements. Wafer scale measurements were possible with no lithography involved as pictured in Figure 4.5. Gold wires were indium cold pressed directly onto the sample(Te cap) surface, and to the sample puck pads. Samples were subsequently inserted into the PPMS.

Longitudinal and transverse resistances R_{xx} and R_{xy} (Figure 4.6) were

4.2. *Transport results showing the conductivity and ferromagnetism in Fe_3GeTe_2 films*

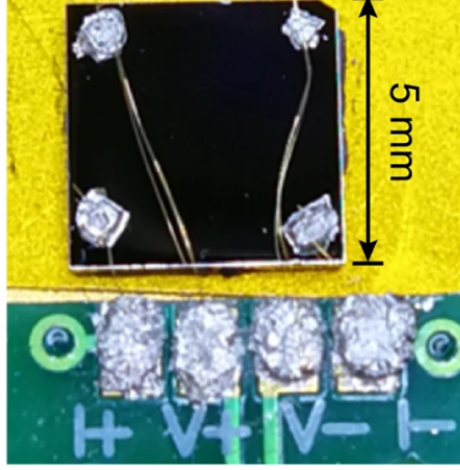


Figure 4.5: A photo of an FGT sample measuring the longitudinal resistance with van der Pauw geometry in a PPMS .

measured on both capped and uncapped samples ranging from 1 QL to 10-QL films. Here it is important to not that the remainder of data corresponds to capped samples unless otherwise stated. Uncapped monolayer and bilayer films did not permit transport measurements due to insulating behavior, likely due to the oxidization of the FGT surface [50]. Differences in transport behavior are negligible between capped and uncapped samples when the thickness $\geq 5QL$. R_{xx} measurements show resistance values consistent with exfoliated samples [24] and indicate a weak insulating behavior at low temperatures in Figure 4.6. In control samples of Te capped Ge substrates (as shown by the purple line in Figure 4.6, we observe a stronger insulating behavior and a much higher resistance than FGT films at low temperatures. Above 200 K, the conduction through Ge substrates is responsible for the higher temperature transition in R_{xx} . The next transition is due to the emergence of localized states with decreasing temperature.

Below 200 K, R_{xx} fit the variable range hopping model in 2D as shown in Figure 4.7, where $R_{xx} \propto e^{T^{-1/3}}$. This is in agreement with previous transport studies [47], which could be attributed to the emergence of localized electrons with decreasing temperature. These localized states likely originate from the Fe 3d orbitals, which are also responsible for the itinerant electrons. The transition temperature (the value at which the hysteresis loop closes agrees well with previous reports of a heavy-fermion state (“lo-

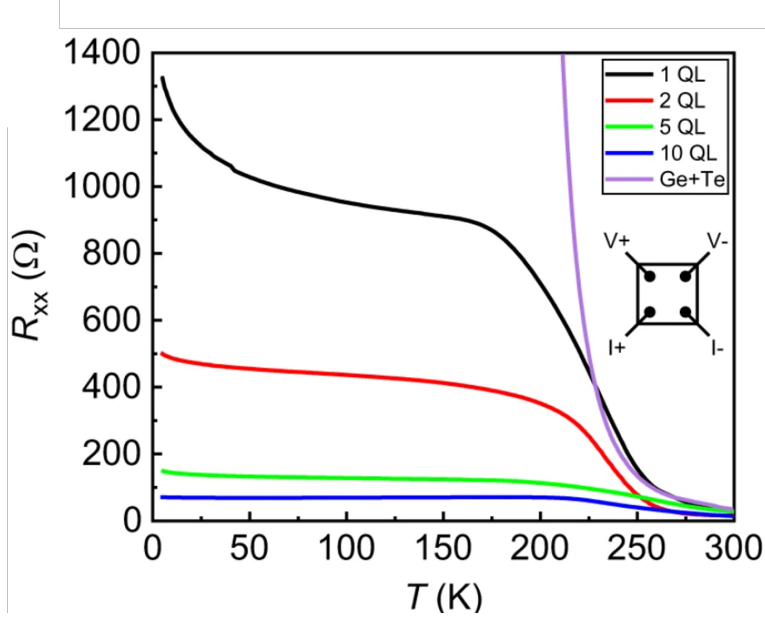


Figure 4.6: Longitudinal resistivity R_{xx} vs. temperature T taken of various QL numbers. A Te capped substrate is also measured as a test sample to see the intrinsic film and cap longitudinal behaviour.

calized”) in bulk [36] and correlated electrons.

4.3 Temperature dependence of the anomalous Hall behavior

To study the phase transition from the FM to paramagnetic state temperature-dependent RAH measurements were carried out on all samples from 5 K to 225 K, as presented in Figure 4.9. Magnetic order was first characterized at 5 K by transverse resistance (R_{xy}) measurements that host the anomalous Hall (AH)

All samples display clear hysteresis indicating ferromagnetic order. 5-QL capped and uncapped samples are shown in Figure 4.8 d, revealing an almost identical remanent (R_R) and saturation resistance (R_S). This implies that, in uncapped samples above 5 QL, the top 1–2 FGT oxide layers do not significantly affect transport properties of the underneath pristine FGT

4.3. Temperature dependence of the anomalous Hall behavior

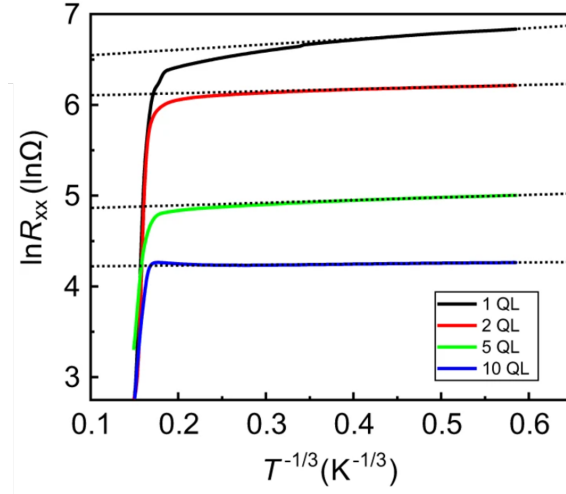


Figure 4.7: Fit of the R_{xx} with the Mott variable range hopping model, indicating the existence of localized states below 125 K.

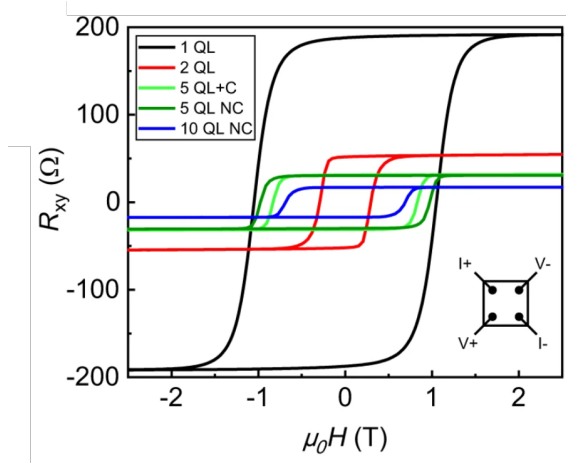


Figure 4.8: R_{AH} vs. applied field of select QL numbers at 5 K showing the AH and hysteresis loops. The applied magnetic field H is perpendicular to the sample surface and parallel to the c axis of FGT. All samples are capped except the two samples marked as non-capped (NC).

4.3. Temperature dependence of the anomalous Hall behavior

layers, suggesting the electronic channels are not confined to the surface. This result is significant considering previous reports of antiferromagnetic coupling between oxidized and pristine FGT, where one would expect uncapped samples to display a two-part hysteresis. We do not observe such a superposition in hysteresis shape. A hole carrier type was determined from R_{xy} at all temperatures. Strong perpendicular magnetic anisotropy (PMA) indicated by the observed textbook-like square shape of the hysteresis. It is important to note that PMA and hysteresis width are proportional [52], and is also indicative of a single domain [52], where all Ising like spins coherently flip at the coercive field (H_C) along the easy axis.

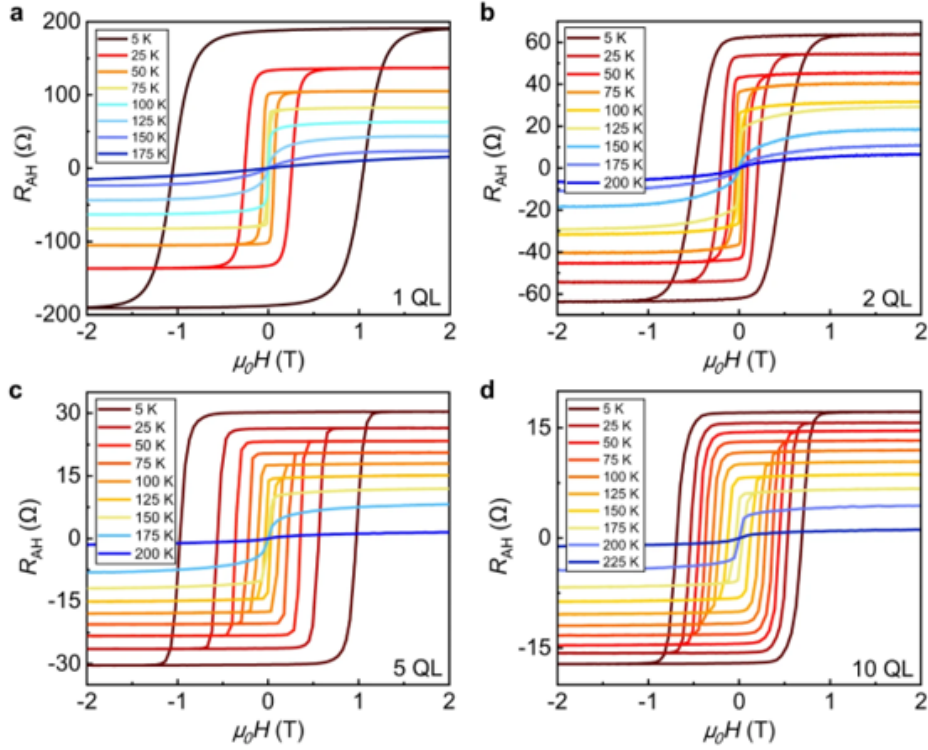


Figure 4.9: Anomalous Hall resistance of a Single-QL, b 2-QL, c 5-QL, and d 10-QL FGT films. The hysteresis loop is apparent in all samples at low temperatures and disappears as the temperature reaches the Curie temperature T_c

4.3. Temperature dependence of the anomalous Hall behavior

From these evolutions we extract various quantities including the coercive field and the remanent and saturation resistance of samples at various temperatures (Figure 4.10). The coercive field (H_C) is defined as the value of the applied magnetic field at which the loop's curve crosses through $R_{AH} = 0$. The remanent and saturation resistance R_R and R_S are defined as the value of R_{AH} at zero applied field and upon saturation, respectively. It is well established that R_R and R_S are directly proportional to the magnetic remanence M_R (the magnetic signal at zero applied field) and magnetic saturation M_S (the magnetic signal when all magnetic moments are maximally aligned) [52]. To investigate the layer and temperature-dependent evolution of the magnetic phases, we compare R_R , R_S , and H_C as a function of layer number at a fixed temperature. With increasing layer number, all samples decrease in the remanent M_R and saturation magnetization M_S Figure 4.10 at a fixed temperature below the respective T_c . This progression is consistent with previous reports [24].

The ratio of R_R and R_S is plotted in Figure 4.10 c. The ratio remains nearly 1 for all QL numbers up to 100 K, where the ratios for 5- and 10-QL samples exceed 0.9 at room temperature. We also note that the energy loss decreases as the layer number is increased, as indicated by the area enclosed by the hysteresis loop after a complete magnetic field sweep.

The field needed to reverse the direction of magnetization, known as the coercive field H_c , provides valuable information for assessing the stability of magnetic structures and is often used as an indication of the hardness of the magnetic domains (Figure 4.10 d). H_C in monolayer samples is greater than 1 T and roughly 0.5, 0.8, and 0.6 T for 2, 5, and 10 QL, respectively. Bilayer samples do not fit into a monotonic decrease of H_C with respect to layer number. One possible explanation is related to hole doping by Fe vacancies, which has been shown to decrease the perpendicular anisotropy [53]. A more thorough layer dependent study is required to reveal the underlying cause. The spin flip transition shown by the gradual progression of R_{AH} around the coercive field could be due to a lack of magnetic anisotropy or the existence of multiple magnetic domains.

T_c is determined by two methods. The remanent resistance R_R serves as a direct probe of spontaneous magnetic order, M_R , and allows us to extract T_c of samples by tracking the temperature at which R_R vanishes (Figure 4.10 f). T_c monotonically increases with layer number. For 1, 2, 5, and 10-QL transitions take place at roughly 75, 125, 150, and 175 K, respectively as compared to 220 in bulk [33]. A secondary method to extract T_c is by Arrott plot analysis [54] (Figure 4.10 e). Arrott plots employ the equa-

4.3. Temperature dependence of the anomalous Hall behavior

h

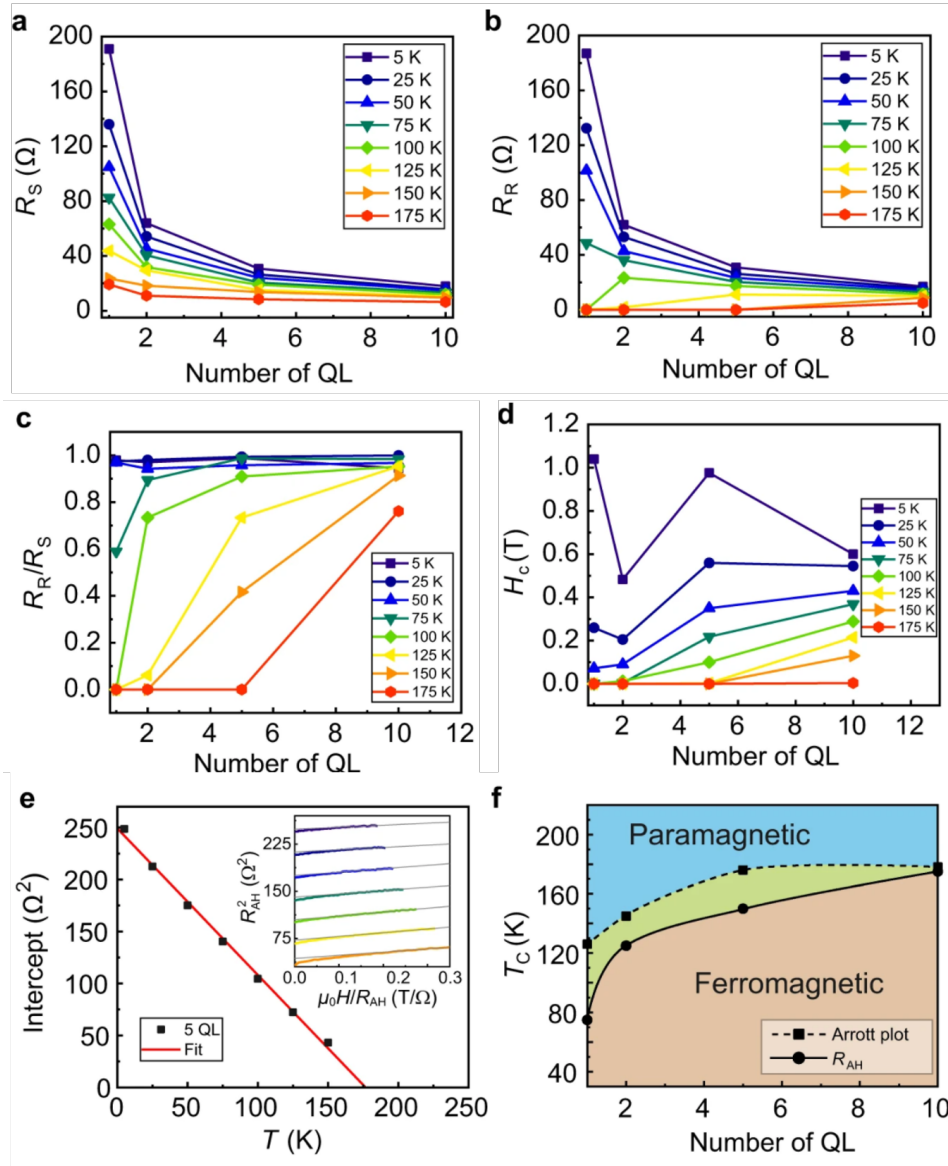


Figure 4.10: a) Remanent resistance (R_R) and b) saturation resistance (R_S) plotted against QL number at various temperatures. Both exhibit a monotonic decrease with increasing layer numbers. c) R_R/R_S ratios remain near unity at different temperatures, suggesting FGTs viability in applications. d) Coercive field (H_c) of various QL layer numbers. e) Arrott plot analysis of a 5-QL sample, indicating a T_c of 176 K extracted by the x-intercept of the fitted line. f) Magnetic phase diagram of FGT as a function of QL number. T_c on the R_{AH} method line is chosen at the lowest temperature at which R_R vanishes in AH measurements. Arrott plot points are found using methods as in e). The green region between the paramagnetic and ferromagnetic state are unmeasured regions where the ferromagnetic state could still survive.

4.3. Temperature dependence of the anomalous Hall behavior

tion $R_{AH} = \mu_0 H / R_{AH}$, from which the high field portion is linearly fitted (inset of Figure 4.10 e). The intercept of R_{AH} is then found for multiple temperatures and again linearly fitted as a function of temperature. The resulting temperature intercept is then used as T_c . This method yields an exact temperature for T_c as compared to the range generated from R_{AH} measurements. Using this method, we have extracted T_c to be 126 K in monolayer samples, 145 K in bilayer samples 176 K, and 178 K in 5 and 10-QL samples, respectively. The two methods show different T_c in samples less than 10-QL, but are in agreement with R_{AH} measurements of 10-QL samples. Upon comparison with the exfoliated layer dependant phase diagram of Deng et al., we see a significant increase in T_c for monolayer and bilayer samples (roughly 100 K increase), but good agreement for 5 and 10-QL samples.

Chapter 5

Discussion & Conclusion

We note that for all layer numbers, FGT retains a strong anisotropy as indicated by the shape of the hysteresis, implying that there is limited hole doping, which has been shown to decrease the magnetocrystalline anisotropy energy and lead to small coercive fields [53]. This is corroborated by bulk sample measurements, which also show strong perpendicular anisotropy [37]. Ultrathin UHV-grown monolayer samples seem to be of significantly higher T_c and more robust ferromagnetism compared to exfoliated samples, as indicated by H_c , R_R/R_S ratio, and the field at which samples saturate indicated by a flat AH signal. We speculate this result is due to damages undergone by the sample during the fabrication process in exfoliation techniques. This is most obvious upon comparison to monolayer hysteresis reported by [24], for example, the coercivity of our epitaxial samples is nearly an order of magnitude larger than exfoliated samples. For monolayer, magnetic saturation was not achieved past 10 T while saturation was reached at only 2 T in exfoliated samples, yet bilayer coercivity samples agree. At low temperatures, the magnetic remanence to magnetic saturation ratio is also much larger in epitaxial samples for layer number less than 5. T_c of monolayer and bilayer samples is higher than any previously reported using anomalous Hall measurements. Effects of domains could play a role in this result. Where the T_c could decrease due to the existence of domains developed to minimize the stray field. Unfortunately in our experiment domains were not directly probed with either Lorentz transmission electron microscopy or magnetic force microscopy thus we cannot make a definite remarks, although the square shape of our hysteresis loop implies single domain across the entire sample. Considering the decrease in coercivity caused by oxidation, indicated by differences in 5-QL capped and uncapped samples, previous monolayer data could be explained by a partially oxidized sample.

The lack of apparent antiferromagnetic interlayer coupling should be discussed with respect to recent reports of systems such as CrI_3 , and CrBr_3 . It is well known that interlayer coupling is extremely sensitive to interlayer distances, which allow for orbital overlap. The considerable distance between adjacent QL containing Fe of roughly 8 Å does not lend itself to strong

interlayer interaction, compared to systems such as CrI_3 where the interlayer distance is smaller (4.2 Å). A recent study using immense pressures revealed that the antiferromagnet-ferromagnet switching is not a result of the interlayer coupling, but due to stacking order differences in CrBr_3 [55].

For FGT, recent DFT, neutron, and spin polarized scanning tunneling microscopy studies [56] the interlayer exchange had been determined to be FM. They show that in calculations it is essential to include the Hubbard U to correctly model interlayer exchange in FGT. In calculations where U is not taken into account the AFM interlayer exchange is energetically favorable, but in systems with nonzero U the FM phase is determined to be the ground state. Furthermore, powder neutron experiments do not show diffraction peaks associated with the AFM phase over a 300 degree window indicating no change in magnetic order across the magnetic phase transition (FM to PM). Lastly, a spin polarized STM does not indicate changes in spin direction across a single layer step edge which would be expected in AFM interlayer exchange.

Looking forward, a recent publication shows the coupling of ferromagnetism and topological states introduces controllable currents in helical edge states in CrI_3 and WTe_2 heterostructures [57], suggesting an interesting future in the heterostructure design of 2D magnetic materials. Future heterostructure design could also be fabricated in techniques enabling control of the relative stacking angle which may pose the possibility to control interlayer interactions and larger superstructure Moire patterns leading to new and exciting spin textures [58].

Planned experiments for FGT include determining the monolayer band structure probed via ARPES to determine the evolution from bulk to monolayer and the search for highly correlated electron behaviour in the existence of flat bands which have been theorized and seen in thicker samples in ARPES experiments [36].

In conclusion, we have synthesized high-quality ultrathin epitaxial FGT (001) films ranging from monolayer to ten layers. The ability to grow at the wafer-scale with precise control of layer number makes production-scale device fabrication a possibility. Epitaxial thin films also allow for the growth of heterostructures and interface engineering in contrast to stacked samples. One particularly important aspect of the growth of thin FGT is that it opens the possibility of interfacial coupling of ferromagnetism with various materials such as superconductors and topological materials.

Bibliography

- [1] K. F. Mak, J. Shan, and D. C. Ralph, “Probing and controlling magnetic states in 2d layered magnetic materials,” *Nature Reviews Physics*, vol. 1, pp. 646–661, Nov 2019.
- [2] D. Zhong, K. L. Seyler, X. Linpeng, R. Cheng, N. Sivadas, B. Huang, E. Schmidgall, T. Taniguchi, K. Watanabe, M. A. McGuire, W. Yao, D. Xiao, K.-M. C. Fu, and X. Xu, “Van der waals engineering of ferromagnetic semiconductor heterostructures for spin and valleytronics,” *Science advances*, vol. 3, pp. e1603113–e1603113, May 2017. 28580423[pmid].
- [3] M. A. McGuire, H. Dixit, V. R. Cooper, and B. C. Sales, “Coupling of crystal structure and magnetism in the layered, ferromagnetic insulator CrI_3 ,” *Chemistry of Materials*, vol. 27, pp. 612–620, Jan 2015.
- [4] I. Tsubokawa, “On the Magnetic Properties of a CrBr_3 Single Crystal,” *Journal of the Physical Society of Japan*, vol. 15, pp. 1664–1668, Sept. 1960.
- [5] M. A. McGuire, G. Clark, S. KC, W. M. Chance, G. E. Jellison, V. R. Cooper, X. Xu, and B. C. Sales, “Magnetic behavior and spin-lattice coupling in cleavable van der waals layered CrCl_3 crystals,” *Phys. Rev. Materials*, vol. 1, p. 014001, Jun 2017.
- [6] H. H. Kim, B. Yang, S. Li, S. Jiang, C. Jin, Z. Tao, G. Nichols, F. Sfigakis, S. Zhong, C. Li, S. Tian, D. G. Cory, G.-X. Miao, J. Shan, K. F. Mak, H. Lei, K. Sun, L. Zhao, and A. W. Tsun, “Evolution of interlayer and intralayer magnetism in three atomically thin chromium trihalides,” *Proceedings of the National Academy of Sciences*, vol. 116, p. 11131, Jun 2019.
- [7] V. K. Joshi, “Multifunctional magnetoelectric materials for device applications.,” *Engineering Science and Technology, an International Journal*, vol. 19, no. 3, pp. 1503–1513, 2016.

- [8] S. J. K. R. Ortega N, Kumar A, “Spintronics: A contemporary review of emerging electronics devices,” *Journal of physics. Condensed matter : an Institute of Physics journal*, vol. 27, no. 50, p. 504002, 2015.
- [9] J.-Y. Bigot, M. Vomir, and E. Beaurepaire, “Coherent ultrafast magnetism induced by femtosecond laser pulses,” *Nature Physics*, vol. 5, pp. 515–520, Jul 2009.
- [10] B. Dieny, “Giant magnetoresistance in spin-valve multilayers,” *Journal of Magnetism and Magnetic Materials*, vol. 136, pp. 335–359, Sep 1994.
- [11] C. Song, B. Cui, F. Li, X. Zhou, and F. Pan, “Recent progress in voltage control of magnetism: Materials, mechanisms, and performance,” *Progress in Materials Science*, vol. 87, pp. 33–82, Jun 2017.
- [12] S. Bhatti, R. Sbiaa, A. Hirohata, H. Ohno, S. Fukami, and S. N. Piramanayagam, “Spintronics based random access memory: a review,” *Materials Today*, vol. 20, pp. 530–548, Nov 2017.
- [13] K. S. Novoselov, A. K. Geim, S. V. Morozov, D. Jiang, Y. Zhang, S. V. Dubonos, I. V. Grigorieva, and A. A. Firsov, “Electric field effect in atomically thin carbon films,” *Science*, vol. 306, p. 666, Oct 2004.
- [14] X. Li, W. Cai, J. An, S. Kim, J. Nah, D. Yang, R. Piner, A. Velamakanni, I. Jung, E. Tutuc, S. K. Banerjee, L. Colombo, and R. S. Ruoff, “Large-area synthesis of high-quality and uniform graphene films on copper foils,” *Science*, vol. 324, p. 1312, Jun 2009.
- [15] Y. Cao, V. Fatemi, S. Fang, K. Watanabe, T. Taniguchi, E. Kaxiras, and P. Jarillo-Herrero, “Unconventional superconductivity in magic-angle graphene superlattices,” *Nature*, vol. 556, pp. 43–50, Apr 2018.
- [16] S. Das, J. A. Robinson, M. Dubey, H. Terrones, and M. Terrones, “Beyond graphene: Progress in novel two-dimensional materials and van der waals solids,” *Annual Review of Materials Research*, vol. 45, pp. 1–27, Jul 2015.
- [17] J. M. Kosterlitz and D. J. Thouless, “Ordering, metastability and phase transitions in two-dimensional systems,” *Journal of Physics C: Solid State Physics*, vol. 6, pp. 1181–1203, Apr 1973.
- [18] N. D. Mermin and H. Wagner, “Absence of ferromagnetism or antiferromagnetism in one- or two-dimensional isotropic heisenberg models,” *Phys. Rev. Lett.*, vol. 17, pp. 1133–1136, Nov 1966.

- [19] X. Xi, Z. Wang, W. Zhao, J.-H. Park, K. T. Law, H. Berger, L. Forró, J. Shan, and K. F. Mak, “Ising pairing in superconducting NbSe₂ atomic layers,” *Nature Physics*, vol. 12, pp. 139–143, Feb 2016.
- [20] D. Huang and J. E. Hoffman, “Monolayer FeSe on SrTiO₃,” *Annual Review of Condensed Matter Physics*, vol. 8, pp. 311–336, Mar 2017.
- [21] E. Sajadi, T. Palomaki, Z. Fei, W. Zhao, P. Bement, C. Olsen, S. Luescher, X. Xu, J. A. Folk, and D. H. Cobden, “Gate-induced superconductivity in a monolayer topological insulator,” *Science*, vol. 362, p. 922, Nov 2018.
- [22] Y. Yu, L. Ma, P. Cai, R. Zhong, C. Ye, J. Shen, G. Gu, X. Chen, and Y. Zhang, “High-temperature superconductivity in monolayer Bi₂Sr₂CaCu₂O_{8+δ},” *Nature*, vol. 575, Nov 2019.
- [23] B. Huang, G. Clark, E. Navarro-Moratalla, D. R. Klein, R. Cheng, K. L. Seyler, D. Zhong, E. Schmidgall, M. A. McGuire, D. H. Cobden, W. Yao, D. Xiao, P. Jarillo-Herrero, and X. Xu, “Layer-dependent ferromagnetism in a van der waals crystal down to the monolayer limit,” *Nature*, vol. 546, pp. 270–273, Jun 2017.
- [24] Y. Deng, Y. Yu, Y. Song, J. Zhang, N. Z. Wang, Z. Sun, Y. Yi, Y. Z. Wu, S. Wu, J. Zhu, J. Wang, X. H. Chen, and Y. Zhang, “Gate-tunable room-temperature ferromagnetism in two-dimensional Fe₃GeTe₂,” *Nature*, vol. 563, pp. 94–99, Nov 2018.
- [25] C. Gong, L. Li, Z. Li, H. Ji, A. Stern, Y. Xia, T. Cao, W. Bao, C. Wang, Y. Wang, Z. Q. Qiu, R. J. Cava, S. G. Louie, J. Xia, and X. Zhang, “Discovery of intrinsic ferromagnetism in two-dimensional van der waals crystals,” *Nature*, vol. 546, pp. 265–269, Jun 2017.
- [26] W. Zhang, P. K. J. Wong, R. Zhu, and A. T. S. Wee, “Van der waals magnets: Wonder building blocks for two-dimensional spintronics?,” *InfoMat*, vol. 1, pp. 479–495, Dec 2019.
- [27] N. Sivadas, M. W. Daniels, R. H. Swendsen, S. Okamoto, and D. Xiao, “Magnetic ground state of semiconducting transition-metal trichalcogenide monolayers,” *Phys. Rev. B*, vol. 91, p. 235425, Jun 2015.
- [28] M. M. Otrokov, I. I. Klimovskikh, H. Bentmann, D. Estyunin, A. Zeugner, Z. S. Aliev, S. Gaß, A. U. B. Wolter, A. V. Koroleva,

- A. M. Shikin, M. Blanco-Rey, M. Hoffmann, I. P. Rusinov, A. Y. Vyzovskaya, S. V. Eremeev, Y. M. Koroteev, V. M. Kuznetsov, F. Freyse, J. Sánchez-Barriga, I. R. Amiraslanov, M. B. Babanly, N. T. Mamedov, N. A. Abdullayev, V. N. Zverev, A. Alfonsov, V. Kataev, B. Büchner, E. F. Schwier, S. Kumar, A. Kimura, L. Petaccia, G. Di Santo, R. C. Vidal, S. Schatz, K. Kißner, M. Ünzelmann, C. H. Min, S. Moser, T. R. F. Peixoto, F. Reinert, A. Ernst, P. M. Echenique, A. Isaeva, and E. V. Chulkov, “Prediction and observation of an antiferromagnetic topological insulator,” *Nature*, vol. 576, pp. 416–422, Dec 2019.
- [29] C. Gong and X. Zhang, “Two-dimensional magnetic crystals and emergent heterostructure devices,” *Science*, vol. 363, p. eaav4450, Feb 2019.
- [30] B. Ding, Z. Li, G. Xu, H. Li, Z. Hou, E. Liu, X. Xi, F. Xu, Y. Yao, and W. Wang, “Observation of magnetic skyrmion bubbles in a van der waals ferromagnet Fe_3GeTe_2 ,” *Nano Letters*, vol. 20, pp. 868–873, Feb 2020.
- [31] Y. Wu, S. Zhang, J. Zhang, W. Wang, Y. L. Zhu, J. Hu, G. Yin, K. Wong, C. Fang, C. Wan, X. Han, Q. Shao, T. Taniguchi, K. Watanabe, J. Zang, Z. Mao, X. Zhang, and K. L. Wang, “Néel-type skyrmion in $\text{WTe}_2/\text{Fe}_3\text{GeTe}_2$ van der waals heterostructure,” *Nature Communications*, vol. 11, p. 3860, Jul 2020.
- [32] H.-J. Deiseroth, K. Aleksandrov, C. Reiner, L. Kienle, and R. K. Kremer, “ Fe_3GeTe_2 and Ni_3GeTe_2 – two new layered transition-metal compounds: Crystal structures, hrtem investigations, and magnetic and electrical properties,” *European Journal of Inorganic Chemistry*, vol. 2006, pp. 1561–1567, Apr 2006.
- [33] N. León-Brito, E. D. Bauer, F. Ronning, J. D. Thompson, and R. Movshovich, “Magnetic microstructure and magnetic properties of uniaxial itinerant ferromagnet Fe_3GeTe_2 ,” *Journal of Applied Physics*, vol. 120, p. 083903, Aug 2016.
- [34] H. L. Zhuang, P. R. C. Kent, and R. G. Hennig, “Strong anisotropy and magnetostriction in the two-dimensional stoner ferromagnet Fe_3GeTe_2 ,” *Phys. Rev. B*, vol. 93, p. 134407, Apr 2016.
- [35] K. Kim, J. Seo, E. Lee, K.-T. Ko, B. S. Kim, B. G. Jang, J. M. Ok, J. Lee, Y. J. Jo, W. Kang, J. H. Shim, C. Kim, H. W. Yeom, B. Il Min, B.-J. Yang, and J. S. Kim, “Large anomalous hall current induced by

- topological nodal lines in a ferromagnetic van der waals semimetal,” *Nature Materials*, vol. 17, pp. 794–799, Sep 2018.
- [36] Y. Zhang, H. Lu, X. Zhu, S. Tan, W. Feng, Q. Liu, W. Zhang, Q. Chen, Y. Liu, X. Luo, D. Xie, L. Luo, Z. Zhang, and X. Lai, “Emergence of kondo lattice behavior in a van der waals itinerant ferromagnet, Fe_3GeTe_2 ,” *Science Advances*, vol. 4, p. eaao6791, Jan 2018.
- [37] C. Tan, J. Lee, S.-G. Jung, T. Park, S. Albarakati, J. Partridge, M. R. Field, D. G. McCulloch, L. Wang, and C. Lee, “Hard magnetic properties in nanoflake van der waals Fe_3GeTe_2 ,” *Nature Communications*, vol. 9, p. 1554, Apr 2018.
- [38] J. Xu, W. A. Phelan, and C.-L. Chien, “Large anomalous nernst effect in a van der waals ferromagnet Fe_3GeTe_2 ,” *Nano Letters*, vol. 19, pp. 8250–8254, Nov 2019.
- [39] M. Alghamdi, M. Lohmann, J. Li, P. R. Jothi, Q. Shao, M. Aldosary, T. Su, B. P. T. Fokwa, and J. Shi, “Highly efficient spin–orbit torque and switching of layered ferromagnet Fe_3GeTe_2 ,” *Nano Letters*, vol. 19, pp. 4400–4405, Jul 2019.
- [40] D. C. Ralph and M. D. Stiles, “Spin transfer torques,” *Journal of Magnetism and Magnetic Materials*, vol. 320, pp. 1190–1216, Apr 2008.
- [41] S. Albarakati, C. Tan, Z.-J. Chen, J. G. Partridge, G. Zheng, L. Farrar, E. L. H. Mayes, M. R. Field, C. Lee, Y. Wang, Y. Xiong, M. Tian, F. Xiang, A. R. Hamilton, O. A. Tretiakov, D. Culcer, Y.-J. Zhao, and L. Wang, “Antisymmetric magnetoresistance in van der waals Fe_3GeTe_2 /graphite/ Fe_3GeTe_2 ; trilayer heterostructures,” *Science Advances*, vol. 5, p. eaaw0409, Jul 2019.
- [42] Z. Fei, B. Huang, P. Malinowski, W. Wang, T. Song, J. Sanchez, W. Yao, D. Xiao, X. Zhu, A. F. May, W. Wu, D. H. Cobden, J.-H. Chu, and X. Xu, “Two-dimensional itinerant ferromagnetism in atomically thin Fe_3GeTe_2 ,” *Nature Materials*, vol. 17, pp. 778–782, Sep 2018.
- [43] E. Karl, “Crucibles, mbe-komponenten <https://www.mbe-komponenten.de>.”
- [44] “9.5: Resistivity,” *Chemistry LibreTexts* <https://chem.libretexts.org>, July 2020.

Bibliography

- [45] A. Graff, M. Thorpe, G. Chair, D. Ghirlanda, S. Matyushov, M. Ozkan, and Treacy, “Network models for materials and biological systems,” 04 2021.
- [46] S. Hasegawa, *Reflection High-Energy Electron Diffraction*, pp. 1–14. American Cancer Society, 2012.
- [47] S. Liu, X. Yuan, Y. Zou, Y. Sheng, C. Huang, E. Zhang, J. Ling, Y. Liu, W. Wang, C. Zhang, J. Zou, K. Wang, and F. Xiu, “Wafer-scale two-dimensional ferromagnetic Fe_3GeTe_2 thin films were grown by molecular beam epitaxy,” *npj 2D Materials and Applications*, vol. 1, 12 2017.
- [48] Y. Hayashi, R. Banal, M. Funato, and Y. Kawakami, “Heteroepitaxy between wurtzite and corundum materials,” *Journal of Applied Physics*, vol. 113, 05 2013.
- [49] D. S. H. Liu, M. Hilse, and R. Engel-Herbert, “Sticking coefficients of selenium and tellurium,” *Journal of Vacuum Science & Technology A*, vol. 39, no. 2, p. 023413, 2021.
- [50] D. Kim, S. Park, J. Lee, J. Yoon, S. Joo, T. Kim, K.-j. Min, S.-Y. Park, C. Kim, K.-W. Moon, C. Lee, J. Hong, and C. Hwang, “Antiferromagnetic coupling of van der waals ferromagnetic Fe_3GeTe_2 ,” *Nanotechnology*, vol. 30, p. 245701, Mar 2019.
- [51] V. Y. Verchenko, A. A. Tsirlin, A. V. Sobolev, I. A. Presniakov, and A. V. Shevelkov, “Ferromagnetic order, strong magnetocrystalline anisotropy, and magnetocaloric effect in the layered telluride Fe_3GeTe_2 ,” *Inorganic Chemistry*, vol. 54, pp. 8598–8607, Sep 2015.
- [52] N. Nagaosa, J. Sinova, S. Onoda, A. H. MacDonald, and N. P. Ong, “Anomalous hall effect,” *Rev. Mod. Phys.*, vol. 82, pp. 1539–1592, May 2010.
- [53] S. Y. Park, D. S. Kim, Y. Liu, J. Hwang, Y. Kim, W. Kim, J.-Y. Kim, C. Petrovic, C. Hwang, S.-K. Mo, H.-j. Kim, B.-C. Min, H. C. Koo, J. Chang, C. Jang, J. W. Choi, and H. Ryu, “Controlling the magnetic anisotropy of the van der waals ferromagnet Fe_3GeTe_2 through hole doping,” *Nano Letters*, vol. 20, pp. 95–100, Jan 2020.
- [54] A. P. Li, J. Shen, J. R. Thompson, and H. H. Weitering, “Ferromagnetic percolation in $\text{Mn}_x\text{Ge}_{1-x}$ dilute magnetic semiconductor,” *Applied Physics Letters*, vol. 86, p. 152507, Apr 2005.

Bibliography

- [55] W. Chen, Z. Sun, Z. Wang, L. Gu, X. Xu, S. Wu, and C. Gao, “Direct observation of van der waals stacking–dependent interlayer magnetism,” *Science*, vol. 366, p. 983, Nov 2019.
- [56] X. Kong, G. D. Nguyen, J. Lee, C. Lee, S. Calder, A. F. May, Z. Gai, A.-P. Li, L. Liang, and T. Berlijn, “Interlayer magnetism in $\text{Fe}_{3-x}\text{GeTe}_2$,” *Physical Review Materials*, vol. 4, Sep 2020.
- [57] W. Zhao, Z. Fei, T. Song, H. K. Choi, T. Palomaki, B. Sun, P. Malinowski, M. A. McGuire, J.-H. Chu, X. Xu, and D. H. Cobden, “Magnetic proximity and nonreciprocal current switching in a monolayer WTe_2 helical edge,” *Nature Materials*, vol. 19, pp. 503–507, May 2020.
- [58] Q. Tong, F. Liu, J. Xiao, and W. Yao, “Skyrmions in the moiré of van der waals 2d magnets,” *Nano Letters*, vol. 18, pp. 7194–7199, Nov 2018.